INTERNATIONAL JOURNAL FOR NUMERICAL METHODS IN FLUIDS
Int. J. Numer. Meth. Fluids 2009; **59**:873–906
Published online 14 July 2008 in Wiley InterScience (www.interscience.wiley.com). DOI: 10.1002/fld.1844

Comparative study of Euler/Euler and Euler/Lagrange approaches simulating evaporation in a turbulent gas–liquid flow

R. Groll[1], S. Jakirlić[2,*,†] and C. Tropea[2]

[1]*Center of Applied Space Technology and Microgravity, Department of Production Engineering, University of Bremen, Am Fallturm, D-28359 Bremen, Germany*
[2]*Chair of Fluid Mechanics and Aerodynamics, Department of Mechanical Engineering, Darmstadt University of Technology, Petersenstrasse 30, D-64287 Darmstadt, Germany*

SUMMARY

This study deals with the Reynolds-averaged Navier–Stokes simulation of evaporation in a turbulent gas–liquid flow in a three-dimensional duct, focussing on the results obtained by a four-equation turbulence model within the framework of the Euler/Euler approach for multiphase flow calculations: in addition to the two-equation $k-\varepsilon$ model describing the turbulence of the continuous (C) phase, the computational model employs transport equations for the turbulence kinetic energy of the disperse (D) phase and for the velocity covariance $q=\langle\{u_i^D\}^D\{u_i^C\}^C\rangle^D$. In the present study, the evaporation model according to Abramzon and Sirignano (*Int. J. Heat Mass Transfer* 1989; **32**:1605–1618) has been extended by introducing an additional transport equation for a newly defined quantity $\overline{a}$, defined as the phase-interface surface fraction. This allows the change in the drop diameter to be quantified in terms of a probability density function. The source term in the equation describing the dynamics of the volumetric fraction of the dispersed phase α^D is related to the evaporation time scale τ_Γ. The performance of the new model is evaluated by performing a comparative analysis of the results obtained by simulating a polydispersed spray in a three-dimensional duct configuration with the results of the Euler/Lagrange calculations performed in parallel. Prior to these calculations, some selected (solid) particle-laden flow configurations were computationally examined with respect to the validation of the background, four-equation, eddy-viscosity-based turbulence model.

Received 22 December 2006; Accepted 17 April 2008

KEY WORDS: gas/liquid flow; Euler/Euler and Euler/Lagrange approaches; four-equation turbulence model; liquid evaporation

*Correspondence to: S. Jakirlić, Chair of Fluid Mechanics and Aerodynamics, Department of Mechanical Engineering, Darmstadt University of Technology, Petersenstrasse 30, D-64287 Darmstadt, Germany.
†E-mail: s.jakirlic@sla.tu-darmstadt.de

Contract/grant sponsor: Publishing Arts Research Council; contract/grant number: 98-1846389

1. INTRODUCTION

Multiphase flows encountered in energy and process engineering are often characterized by a phase interchange due to dispersed phase evaporation. When simulating the motion of liquid drops in a dry gas, it is important to capture not only the evaporation but also the interaction between the discrete and continuous phases. For instance, strong evaporation rates at the interfacial surface and the relative humidity influence the shear stress dynamics at the interface and the overall droplet drag in the air flow. Typical applications include direct injection of a diesel spray (break-up, evaporation and combustion are occurring sequentially), spray drying in the foodstuff or pharmaceutical industries or spray painting. These are only a few illustrative examples for industrial research areas, which use powerful optimization tools for the prediction of multiphase transport processes. The capability of a computational scheme to account for all important phenomena featuring these processes is a major prerequisite for successful design and optimization of many industrial, multiphase systems.

Commonly used computational schemes describing the interaction between the continuous carrier phase and a particulate phase in such multiphase processes are the Euler/Lagrange and the Euler/Euler approaches. The most widely used approach in technical applications is the Euler/Lagrange method, which solves the governing equations only for the carrier phase. In this concept, the associated dispersed (here liquid) phase is accounted for by solving the equations of motion of single droplets (i.e. droplet parcels) and their positions (droplet trajectories) within the continuous phase flow field (Lagrangian algorithm). The coupling between phases is accomplished through the source terms in the equations governing the carrier phase, which account for the mass, momentum and heat exchange. An important advantage of this approach is its numerical stability and robustness. One disadvantage of the Euler/Lagrange approach is the high computational load, since individual particle tracking necessitates a time-resolved solution procedure. In an alternative approach, known as the Euler/Euler approach, the motion of both phases, regarded as two inter-penetrating continua, are described by a particular set of transport equations that governs both phases. Conceptually, this approach is more straightforward than the Euler/Lagrange method, making it attractive for industrial applications. New variables α^C and α^D, called the volume fractions of the continuous (C) and the dispersed phase (D), are introduced in this method. The sum of the volume fraction of all participating phases is equal: $\sum_k \alpha^k = 1$ ($k = C, D$). The convective terms and volumetric fraction–velocity correlations $\overline{\alpha^k u_i^k} = \overline{\alpha^k}\langle u_i^k \rangle^k$ are described with the help of a volumetric-fraction-weighted averaging operator $\langle . \rangle^k$, see e.g. Politis [1]. The Euler/Euler approach is numerically more demanding, mainly due to fact that higher-order convective schemes must be employed in order to solve correctly the corresponding continuity equation exhibiting hyperbolic-type behavior due to lack of any diffusion-like term. Recently, Oliveira and Issa [2] addressed some numerical difficulties associated with the solution algorithm used in the framework of the Eulerian approach, pertinent mostly to the possible vanishing tendency of the volume fractions α in different situations (e.g. phase segregation, recirculating flows) and proposed useful remedies.

A large number of statistical turbulence models for single-phase flows defining the Reynolds stress tensor, whose gradients originate from the (convective) turbulent transport of momentum, have been developed in the past. The most widely used are those based on Boussinesq's analogy

DOI: 10.1002/fld

employing eddy viscosity as the model parameter,[‡] whose formulation was provided in the framework of the standard $k-\varepsilon$ modelling concept [7]. In that case, dynamic equations for the turbulent kinetic energy k and its viscous dissipation rate ε are employed. The analog equation set for continuous phase in a two-phase flow differs through several additional production and destruction (sink) terms arising from the drag interaction process. The eddy viscosity model group generally 'transforms' the Reynolds stress gradient into a diffusion-like transport term. Such a diffusion term does not result from the interaction between turbulent eddies in the two-phase flows; here, turbulent transport has a somewhat different nature due to non-viscous character of the particles. The turbulent motion of particles is represented by mixing of particle clouds. The turbulence quantities characterizing the dispersed phase are most often obtained either from the one-equation model scheme (transport equation for k^D and an algebraic relationship for the corresponding dissipation rate) or from appropriate algebraic formulations. In the present study, a different procedure was adopted, in line with the model proposed by He and Simonin [8]. Besides transport equations for the turbulent kinetic energy of the dispersed phase k^D, the model employs a transport equation for the velocity covariance $q=\langle\{u_i^D\}^D\{u_i^C\}^C\rangle^D$, being another variable representing a sink of turbulence, instead of dissipation rate, whose existence as a viscous-dependent variable is not always possible, as e.g. in the case of solid particles, due to their non-viscous character.

General studies according to Clift *et al.* [9] and Crowe *et al.* [10] introduce a couple of partial models describing effects dominating the droplet-laden gaseous flows. Additional terms describing momentum and turbulence sources are introduced with respect to modelling the diffusion (e.g. Crowe *et al.* [11]) and dissipation rate. The drag force is formulated in terms of the characteristic drag relaxation time scale τ_{p}^k, which depends on the Reynolds number based on the difference of particle and carrier phase velocities [12]. The interactions between the dispersed particle phase and the continuous carrier phase [13] itself and the particle/wall and inter-particle collisions are approximated by models based on the eddy diffusivity approach for the particle velocity fluctuations [14, 15]. The modification of Grad's theory according to Jenkins and Richman [16] is based on the definition of a constant elasticity coefficient e_{c}, which describes the influence of particle elasticity on turbulent particle momentum diffusion and turbulence dissipation. The local diffusion induced by crossing trajectory effects depending on local particle flux, which is not resolved by particle mean velocity, was modelled by Csanady [17]. A very comprehensive overview of the multiphase flow modelling methods including also direct numerical simulation and probability density function (PDF) models and a number of computational examples is given in the study of Loth *et al.* [18].

The models of the turbulent diffusion and dissipation derived for solid particle motion can be adopted for predicting a liquid polydispersed phase in a humid carrier gas phase. The computational description of the evaporation process requests the calculation of the heat and mass transfer exchange rate over the liquid/gas interface. The parameter influencing mostly these exchange rates is the relative humidity of the gas phase. The highest gradient of relative humidity occurs at the temperature levels slightly below the boiling point. Because of that, these temperatures

[‡]The models based on solution of the transport equations for each component of the Reynolds stress tensor $\overline{u_i u_j}$—differential second-moment closures (SMC)—are much rarely applied in conjunction with two-phase flow calculations. We mentioned here only some relevant publications: Lopez de Bertodano *et al.* [3], Lance *et al.* [4], Chen and Pereira [5] and Vit *et al.* [6].

DOI: 10.1002/fld

have to be accounted for when computing the dispersed phase evaporation driven by temperature increase. The dimensionless numbers characterizing the heat and mass exchange process are the Nusselt number Nu and the Sherwood number Sh. Several models, e.g. [19, 20], based on the correlation model of Ranz and Marschall [21], have been developed to model these parameters. The evaporation rate model of Abramzon and Sirignano [22] considers additionally the latent heat flux of the evaporated liquid leaving the droplet. The correct capturing of the gas-phase humidity requires the liquid vapor mass ratio Y, influenced by convective, conductive, turbulent and thermal diffusive effects, to be computed from an appropriate transport equation in addition to the equation governing the temperature field T. Additionally, evaporation and thermal diffusion are prescribed by the drop number density or the phase interface area. The latter variable is defined by number density of the dispersed phase and its mean drop surface. In order to calculate this area per volume, the PDF of the drop diameter of the polydispersed phase has to be specified. Based on the d^2-law, which means that the drop surface of a spherical drop decreases linearly during the evaporation process, and the drop diameter PDF, the heat and mass transfers of the evaporating polydispersed liquid phase can be simulated.

The following studies dealing with the numerical calculation of flow configurations accounting for the evaporation process are to be mentioned. Sommerfeld *et al.* [23] performed complementary experimental and numerical investigations of a spray evaporating in a heated air flow. In this study a short overview of the most widely used evaporation models was also given. The calculations were conducted applying the $k-\varepsilon$ model for the gaseous phase. The interaction with the droplet phase was accounted for in the framework of the Lagrangian approach. The evaporation model of Abramson and Sirignano assuming the infinite droplet conductivity was applied to account for the rapid evaporation due to blowing effects. Chen and Pereira [5] have simulated the evaporation in a turbulent spray flow. The computational method used was based on a full Reynolds stress model. The turbulent diffusion modelling of the spray phase relied on the eddy dissipation ansatz with respect to the continuous carrier phase. The evaporation algorithm accounted for the unsteady simulation of the droplet transport. Two model formulations were compared, one based on the standard Sherwood number and the other based on the modified Sherwood number as proposed by Abramzon and Sirignano [22]. Aggarwal and Park [24] described computationally the increase in the humidity in a laminar swirling jet flow. The diameter decrease is modelled by a time-dependent algorithm, which makes an unsteady simulation necessary. Klingsporn and Renz [25] compared the results of their calculations utilizing the jet length model of Abramzon and Sirignano [22] with experimental data taken from a high pressure rig. Gosman and Clerides [26] scrutinized the performance of different evaporation models describing the evaporation rate by modelling the Sherwood and Nusselt numbers appropriately. Hereby, mutual comparison of the model results focussing on the influence of the interphase heat transfer on the evaporation rate itself was provided. Very recently, Kolaitis and Founti [27] performed a comparative assessment of a number of droplet evaporation models regarding their physical accuracy and numerical robustness and efficiency, and the latter with respect to the model performance when implemented in a computational fluid dynamics (CFD) code. The computational examples serving for this analysis ranged from a single droplet evaporating in a constant temperature and constant velocity air flow to a multiphase flow system in a suddenly expanded pipe configuration consisting of a liquid spray issuing downward from a hollow cone nozzle surrounded by a co-flowing turbulent air stream. The latter experimental investigations were conducted by Sommerfeld and Qiu [28].

In the present study, the evaporation model according to Abramzon and Sirignano [22] is extended to account for the dynamics of a newly defined variable, called the phase-interface surface

DOI: 10.1002/fld

fraction. Herewith, the quantification of the droplet diameter in terms of a PDF is enabled. This new model scheme is validated by performing the Reynolds-averaged Navier–Stokes (RANS) calculation of a spray evaporating in a three-dimensional duct flow. Hereby, the focus is on the comparative analysis of the results obtained by Euler/Euler and Euler/Lagrange computational strategies. Prior to these calculations, the background, four-equation, eddy viscosity turbulence model was validated through computations of the particle-laden, fully developed channel flow (e.g. Kulick *et al.* [29]) and the flow over a backward-facing step (e.g. Fessler and Eaton [30]). In addition, the results obtained were also compared with the results of the complementary Euler/Lagrange computations according to Kohnen [31].

2. COMPUTATIONAL MODEL

This section outlines the background computational model used in the present study. The Favré-averaged form of the Reynolds-averaged equations describing the transport of mass, momentum, heat, species and turbulent quantities of a continuous and a disperse phase interacting with each other in the two-fluids, Euler/Euler framework are presented. Instead of using density, all equations are weighted by the volumetric fraction α^k (superscript k stands for C—continuous phase and D—discrete phase; $\overline{C}=D$, $\overline{D}=C$, $\alpha^C+\alpha^D=1$; note that the overbar denotes '*complement*' in these expressions, unlike an '*average*' elsewhere).

The volume fraction averaging procedure applied on an arbitrary variable $\phi(=\bar{\phi}+\phi')$ is defined as follows, with $\{\phi\}^k$ representing its fluctuation about the averaged value $\langle\phi\rangle^k$ (see e.g. Politis [1]):

$$\langle\phi\rangle^k=\frac{\overline{\alpha^k\phi}}{\bar{\alpha}^k},\quad \{\phi\}^k=\phi-\langle\phi\rangle^k \tag{1}$$

$$\bar{\alpha}^k\langle\phi\rangle^k=\overline{\alpha^k\phi}=\overline{\alpha^k(\bar{\phi}+\phi')}=\bar{\alpha}^k\bar{\phi}+\overline{\alpha^k\phi'} \tag{2}$$

The rationale of this kind of averaging will be further outlined by presenting the mass balance in a two-phase flow.

2.1. Mass balance

The continuity equation corresponding to the instantaneous flow field reads

$$\frac{\partial}{\partial t}(\rho^k\alpha^k)+\frac{\partial}{\partial x_i}(\rho^k\alpha^k u_i^k)=\Gamma^k\quad \text{with } k\in\{C,D\} \tag{3}$$

The source term Γ^k in Equation (3), representing actually the mass transfer rate, originates from the phase exchange due to evaporation process and represents certainly one of the most important parts of the computational model. The sum of the specific mass source terms Γ^D and Γ^C of dispersed and continuous phase has to take zero value: $\Gamma^C+\Gamma^D=0$.

The volumetric fraction–velocity correlation $\overline{\alpha^k u_i^k}=\bar{\alpha}^k\langle u_i^k\rangle$ arises after applying the volume fraction averaging procedure on the convective term in Equation (3). The resulting equation takes the following form:

$$\partial_t(\rho^k\bar{\alpha}^k)+\partial_j(\rho^k\bar{\alpha}^k\langle u_j^k\rangle^k)=\overline{\Gamma}^k\quad \text{where } \overline{\Gamma}^C+\overline{\Gamma}^D=0 \tag{4}$$

DOI: 10.1002/fld

2.1.1. Difference between the Reynolds and volume-weighted averaging filters. The following expression results when applying the rule given by Equation (2) on the velocity field:

$$\Delta_i^k = \langle u_i^k \rangle^k - \bar{u}_i^k = \frac{\overline{\alpha^k u_i^{k\prime}}}{\bar{\alpha}^k} \tag{5}$$

Deutsch and Simonin [32] modelled the correlation of volumetric fraction and velocity fluctuation appearing on the right-hand side of Equation (5) by applying a simple gradient diffusion hypothesis $\overline{\alpha^k u_i^{k\prime}} = -\nu_\alpha \partial_j \bar{\alpha}^k$, with ν_α representing an isotropic diffusion coefficient. Substituting this diffusion model into the mass balance equation (4) the following form of the equation governing the volumetric fraction of dispersed and continuous phase is obtained:

$$\frac{\partial}{\partial t}(\rho^k \bar{\alpha}^k) + \frac{\partial}{\partial x_i}(\rho^k \bar{\alpha}^k \bar{u}_i^k) = \bar{\Gamma}^k + \frac{\partial}{\partial x_i}\left(\rho^k \nu_\alpha \frac{\partial \bar{\alpha}^k}{\partial x_i}\right) \tag{6}$$

The diffusion coefficient ν_α is defined via mass diffusion time scale τ_α and velocity covariance $q = \langle \{u_i^C\}^C \{u_i^D\}^D \rangle^D$, the latter representing the trace of the velocity vector correlation tensor of both phases:

$$\nu_\alpha = \tfrac{1}{3}\tau_\alpha q \tag{7}$$

with τ_α proposed by Csanady [17]:

$$\tau_\alpha = \tau_t^C \sqrt{1 + C_\beta \xi_r^2} \quad \text{with } C_\beta = 0.45, \quad \xi_r = \sqrt{\frac{(\langle \mathbf{u}^D \rangle^D - \langle \mathbf{u}^C \rangle^C)^2}{\frac{2}{3}k^D}} \tag{8}$$

depending on the turbulent kinetic energy of the dispersed phase and the turbulent time scale of the continuous phase

$$k^D = \frac{1}{2}\langle \{u_i^D\}^D \{u_i^D\}^D \rangle^D, \quad \tau_t^C = \frac{3}{2} C_\mu \frac{k^C}{\varepsilon_{\mathrm{M}}^C} \quad \text{with } C_\mu = 0.09 \tag{9}$$

Herewith, the equation governing the mass balance in a two-phase flow, featuring the dependency of the volumetric fractions on velocity and turbulence intensity of dispersed and continuous phase, is closed, if the turbulent quantities of both phases are known.

2.2. Attaching forces

The particle number density n representing the number of particles per volume

$$n = \lim_{V \to V_0} \frac{N_V}{V} \tag{10}$$

is defined by the volumetric fraction α^D and the expectation of the particle diameter cube assuming a spherical particle:

$$\alpha^D = n\, E(V_{\mathrm{p}}) = n \frac{\pi E(D_{\mathrm{p}}^3)}{6} \quad \Rightarrow \quad n = \frac{\alpha^D}{V_{\mathrm{p}}} = \frac{6\alpha^D}{\pi E(D_{\mathrm{p}}^3)} \tag{11}$$

DOI: 10.1002/fld

Accordingly, the gravity and lift forces can be defined as follows:

$$\mathbf{F}_{\mathrm{G}}\cdot n=\rho^{D}E(V_{\mathrm{p}})n\mathbf{g}=\rho^{D}\alpha^{D}\mathbf{g},\quad \mathbf{F}_{\mathrm{L}}\cdot n=-\alpha^{D}\nabla p \tag{12}$$

The drag force on a spherical particle depending on the relative particle Reynolds number

$$\mathbf{F}_{D}=3\pi\mu^{C}\mathbf{U}_{\mathrm{rel}}\frac{E(D_{\mathrm{p}}^{3})}{E(D_{\mathrm{p}}^{2})}(1+0,15Re_{\mathrm{rel}}^{0,687}) \tag{13}$$

$$Re_{\mathrm{rel}}=\frac{\rho^{C}E(D_{\mathrm{p}})|\langle\mathbf{u}^{C}\rangle^{C}-\langle\mathbf{u}^{D}\rangle^{D}|}{\mu^{C}} \tag{14}$$

has to be multiplied with the particle number to formulate the volume-specific drag force of the dispersed phase:

$$\rho^{D}f_{i}=F_{Di}\cdot n=\frac{\rho^{D}\alpha^{D}}{\tau_{\mathrm{p}}}(u_{i}^{C}-u_{i}^{D}) \tag{15}$$

$$\tau_{\mathrm{p}}=\frac{\rho^{D}E(D^{2})}{18\,\mu^{C}}(1+0.15\,Re_{\mathrm{rel}}^{0.687})^{-1} \tag{16}$$

The drag relaxation time scale τ_{p} depends on the expectation value of the squared diameter and the relative Reynolds number [10].

Although the Reynolds averaging of the lift and gravity forces produces no additional terms, the averaging of the drag force results in an additional term depending on filter difference Δ_{i}^{C} (see Equation (5)):

$$\frac{\rho^{D}\bar{\alpha}^{D}}{\tau_{\mathrm{p}}}(\langle u_{i}^{C}\rangle^{D}-\langle u_{i}^{D}\rangle^{D})=\frac{\rho^{D}\bar{\alpha}^{D}}{\tau_{\mathrm{p}}}\left(\langle u_{i}^{C}\rangle^{C}-\langle u_{i}^{D}\rangle^{D}-\frac{\Delta_{i}^{C}}{\bar{\alpha}^{D}}\right) \tag{17}$$

The latter term arises from the inequality of both the volume-weighted filters:

$$\langle\phi\rangle^{D}-\langle\phi\rangle^{C}=\frac{\bar{\alpha}^{C}\overline{\alpha^{D\prime}\phi^{\prime}}+\bar{\alpha}^{D}\overline{\alpha^{D\prime}\phi^{\prime}}}{\bar{\alpha}^{C}\bar{\alpha}^{D}}=\frac{\overline{\alpha^{D\prime}\phi^{\prime}}}{\bar{\alpha}^{C}\bar{\alpha}^{D}} \tag{18}$$

The transport of momentum of both phases has to account for the corresponding filters. As analyzed in the study of Oliveira [33], this additional source term represents an expected outcome of the modelling approach of the momentum equations governing both $\langle u_{i}^{C}\rangle^{C}$ and $\langle u_{i}^{D}\rangle^{D}$.

2.3. Momentum transport

In the present study, the Reynolds stress tensor, that is the fluctuating velocity correlation in the momentum equation, is modelled by using the Boussinesq formulation within the eddy viscosity modelling concept:

$$-\langle\{u_{i}^{k}\}^{k}\{u_{j}^{k}\}^{k}\rangle^{k}=\nu_{t}^{k}(\partial_{j}\langle u_{i}^{k}\rangle^{k}+\partial_{i}\langle u_{j}^{k}\rangle^{k}-\tfrac{2}{3}\,\partial_{l}\langle u_{l}^{k}\rangle^{k}\delta_{ij})-\tfrac{2}{3}k^{k}\delta_{ij} \tag{19}$$

DOI: 10.1002/fld

The turbulent viscosity of the continuous phase v_t^C is approximated in line with the k–ε model of Jones and Launder [7] as follows:

$$v_t^C = C_\mu \frac{(k^C)^2}{\varepsilon_{\mathrm{M}}^C}, \quad k^C = \frac{1}{2}\langle\{u_i^C\}^C\{u_i^C\}^C\rangle^C \tag{20}$$

Although the turbulent viscosity of the continuous phase is defined by turbulent time scales ($k^C/\varepsilon_{\mathrm{M}}^C$) only, the diffusion coefficient of the dispersed phase v_t^D is function of the mass diffusion v_α, the drag relaxation time scale τ_{p} and the particle collision time scale τ_{c},

$$v_t^D = \frac{v_\alpha + \frac{1}{3}\tau_{\mathrm{p}} k^D}{1 + 0.4\tau_{\mathrm{p}}/\tau_{\mathrm{c}}}, \quad k^D = \frac{1}{2}\langle\{u_i^D\}^D\{u_i^D\}^D\rangle^D \tag{21}$$

the latter depending on the collision rate $\dot{N}$ ($\equiv n A_n v_n$, $A_n = \pi D_{\mathrm{p}}^2$):

$$\tau_{\mathrm{c}} = \frac{1}{\dot{N}} = (n\pi D_{\mathrm{p}}^2 v_n)^{-1} \tag{22}$$

Furthermore, the collision velocity v_n is formulated in line with the proposal of He and Simonin [8]:

$$v_n = \sqrt{\frac{16}{\pi}\frac{2}{3}k^D} = \frac{4}{\pi^{1/2}} u_{\mathrm{rms}}^D \approx 2.2568 u_{\mathrm{rms}}^D \tag{23}$$

Substituting the expressions for collision velocity v_n and particle number n (Equation (11)) into Equation (22) the collision time scale, representing the number of collisions of a single particle per time, can be finally formulated as follows:

$$\tau_{\mathrm{c}}^{-1} = 6\bar{\alpha}^D \frac{E(D_{\mathrm{p}}^2)}{E(D_{\mathrm{p}}^3)} \sqrt{\frac{16}{\pi}\frac{2}{3}k^D} \tag{24}$$

The ratio of the expected values of the particle diameter cube to the particle diameter square in Equation (24) represents the Sauter mean diameter D_{32}.

The final form of the equation governing the momentum of both the dispersed and the continuous phase reads

$$\begin{aligned}
&\partial_t(\rho^k \bar{\alpha}^k \langle u_i^k\rangle^k) + \partial_j(\rho^k \bar{\alpha}^k \langle u_i^k\rangle^k \langle u_j^k\rangle^k) \\
&\quad = \rho^k \bar{\alpha}^k g_i - \bar{\alpha}^k \partial_i \langle p\rangle^k + \partial_j((\mu^k + \mu_t^k)\bar{\alpha}^k(\partial_j\langle u_i^k\rangle^k + \partial_i\langle u_j^k\rangle^k - \tfrac{2}{3}\partial_l\langle u_l^k\rangle^k\delta_{ij})) \\
&\qquad -\partial_i\left(\rho^k\bar{\alpha}^k\frac{2}{3}k^k\right) + \frac{\rho^D\bar{\alpha}^D}{\tau_{\mathrm{p}}}(\langle u_i^{\bar{k}}\rangle^{\bar{k}} - \langle u_i^k\rangle^k) + \frac{\rho^D}{\tau_{\mathrm{p}}}\Delta_i^C \cdot \mathrm{sign}(k)
\end{aligned} \tag{25}$$

where

$$\mathrm{sign}(C) = 1, \quad \mathrm{sign}(D) = -1, \quad \mathrm{sign}(\bar{k}) = -\mathrm{sign}(k) \tag{26}$$

The turbulence model equations governing the quantities k^D, q as well as k^C and $\varepsilon_{\mathrm{M}}^C$ are given in Section 2.8.

DOI: 10.1002/fld

2.4. Evaporation-dependent diameter PDF

In an evaporating process, the mass transfer rate on the drop surface depends on the drop size. The polydispersed spray consists of drops with different diameters. To determine the mass transfer, i.e. the evaporation rate for such a case, the drop diameter distribution of the spray is necessary. Using the approach based on a particle diameter PDF (see Figure 1 for its graphical representation)

$$f\left(\frac{D_\mathrm{p}}{E(D_\mathrm{p})}\right)=\frac{\pi}{2}\frac{D_\mathrm{p}}{E(D_\mathrm{p})}\,\mathrm{e}^{-(\pi/4)D_\mathrm{p}^2/E(D_\mathrm{p})^2} \quad \text{with } f(D_\mathrm{p})=\frac{9}{8}\pi\frac{D_\mathrm{p}}{D_{32}^2}\,\mathrm{e}^{-(9/16)\pi D_\mathrm{p}^2/D_{32}^2} \tag{27}$$

depending on the Sauter mean diameter,

$$D_{32}=\frac{E(D_\mathrm{p}^3)}{E(D_\mathrm{p}^2)}=\frac{6\bar{\alpha}^D}{\bar{a}} \tag{28}$$

with the newly defined variable $\bar{a}$ being the phase-interface surface fraction; the mass transfer rate can be calculated [34]. The expectation values of the squared and cubic diameters only in terms of the Sauter mean diameter result from this modelled PDF:

$$E(D_\mathrm{p})=\frac{2}{3}D_{32},\quad E(D_\mathrm{p}^2)=\frac{16}{9\pi}D_{32}^2,\quad E(D_\mathrm{p}^3)=\frac{16}{9\pi}D_{32}^3 \tag{29}$$

A time-dependent relation has to be defined to calculate the change of the drop diameter when simulating motion of a polydispersed phase. The change of the expectation value of the diameter squared is presumed to be constant in accordance with the d^2-law [35]:

$$\frac{\mathrm{d}}{\mathrm{d}t}E(D_\mathrm{p}^2)=-\Gamma \tag{30}$$

Integration of this equation results in the time-dependent solution for the drop diameter:

$$D_\mathrm{p}(t)=\sqrt{D_\mathrm{p}^2(0)-\Gamma t} \tag{31}$$

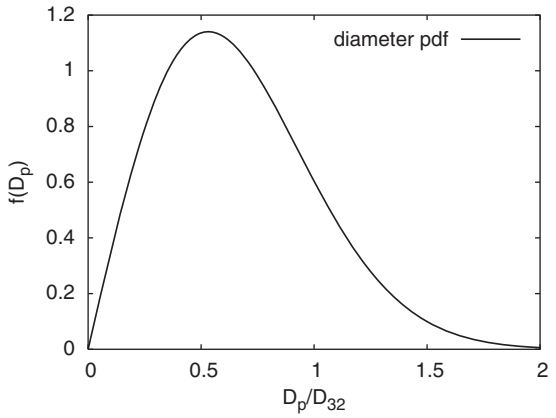

Figure 1. PDF of a normalized particle drop diameter in a polydispersed spray.

DOI: 10.1002/fld

Substitution of the expectation value with the given density function definition

$$-\Gamma=\frac{\mathrm{d}}{\mathrm{d}t}E(D_{\mathrm{p}}^2)=\frac{16}{9\pi}\frac{\mathrm{d}}{\mathrm{d}t}D_{32}^2=\frac{32}{9\pi}\dot{D}_{32}\frac{\mathrm{d}}{\mathrm{d}t}D_{32}\Rightarrow\dot{D}_{32}=-\frac{9\pi}{32}\frac{\Gamma}{D_{32}} \tag{32}$$

reveals that the deviation of the Sauter mean diameter depends on the evaporation constant of the d^2-law. Based on this formulation, the following equation has been derived:

$$\frac{\mathrm{d}}{\mathrm{d}t}E(D_{\mathrm{p}}^3)=\frac{16}{9\pi}\frac{\mathrm{d}}{\mathrm{d}t}D_{32}^3=\frac{16}{9\pi}\left(\dot{D}_{32}D_{32}^2+D_{32}\frac{\mathrm{d}}{\mathrm{d}t}D_{32}^2\right)=-\frac{3}{2}\Gamma D_{32} \tag{33}$$

With this expression, the time-dependent change of an expected drop volume is defined. The outcome of the last equation is used for the determination of the mass transfer of a drop with the expected mass $\bar{m}_{\mathrm{p}}$:

$$\frac{\mathrm{d}\bar{m}_{\mathrm{p}}}{\mathrm{d}t}=\frac{\pi}{6}\rho^D\frac{\mathrm{d}}{\mathrm{d}t}E(D_{\mathrm{p}}^3)=-\frac{\pi}{4}\rho^D D_{32}\Gamma \tag{34}$$

Based on the evaporation model according to Abramzon and Sirignano [22], the mass transfer rate at the surface of a drop cloud representing a function of the modified Sherwood number Sh^* and the mass transfer coefficient B_{M} is to be determined by using the following equation:

$$\dot{m}=\pi D_{21}\rho^C D_{\alpha\beta}Sh^*\ln(1+B_{\mathrm{M}}) \tag{35}$$

The definitions of the Sherwood number and its modification and the mass transfer coefficient are given in Section 3. By equalizing the PDF-dependent mass transfer rate and the modelled mass transfer rate, the evaporation constant in the model of Abramzon and Sirignano [22] is defined as

$$\begin{aligned}&\frac{\pi}{4}\rho^D D_{32}\Gamma=-\dot{m}_{\mathrm{p}}=\dot{m}=\pi D_{21}\rho^C D_{\alpha\beta}Sh^*\ln(1+B_{\mathrm{M}})\\&\Rightarrow\Gamma=4\frac{D_{21}}{D_{32}}\frac{\rho^C}{\rho^D}D_{\alpha\beta}Sh^*\ln(1+B_{\mathrm{M}})\end{aligned} \tag{36}$$

In accordance with the d^2-law, the evaporation constant should be independent of the particle diameters. This fact brings an additional constraint to the expectation values of the probability function: $D_{21}/D_{32}=$const. The given PDF fulfills this condition as follows:

$$\frac{D_{21}}{D_{32}}=\frac{E(D^2)E(D^2)}{E(D)E(D^3)}=\frac{8}{3\pi} \tag{37}$$

With the proposal of Abramzon and Sirignano, the time-dependent modelling of the drop diameter probability function is closed.

2.5. Evaporation progress

The model developed serves for calculation of the evaporation rate of spherical water drops. Water is a liquid dispersed phase that satisfies the d^2-law. Keeping in mind the definition of the life time of a drop T and its diameter loss rate, it is known that each drop with a diameter

$$D_{\mathrm{p}}<(\Gamma T)^{1/2} \tag{38}$$

DOI: 10.1002/fld

is evaporated completely. To determine the number of evaporated drops in a cloud, the PDF has to be integrated in the following manner:

$$\int_0^{(\Gamma T)^{1/2}} f(D_\mathrm{p})\,\mathrm{d}D_\mathrm{p} \tag{39}$$

Consequently, the time change of the particle number is obtained as follows:

$$\frac{\mathrm{d}\bar{n}}{\mathrm{d}t} = -\lim_{\mathrm{T}\to 0}\left[\frac{\bar{n}}{T}\int_0^{(\Gamma T)^{1/2}} f(D_\mathrm{p})\,\mathrm{d}D_\mathrm{p}\right] = \lim_{\mathrm{T}\to 0}\left[\frac{\bar{n}}{T}(\mathrm{e}^{-(9\pi/16)\Gamma T/D_{32}^2}-1)\right] \tag{40}$$

$$= \lim_{\mathrm{T}\to 0}\left[\frac{\bar{n}}{T}(\mathrm{e}^{mT}-1)\right], \quad m = -\frac{9\pi}{16}\frac{\Gamma}{D_{32}^2}$$

$$= \lim_{\mathrm{T}\to 0}\left[\frac{\bar{n}}{T}((1+mT)^{1/mT\cdot mT}-1)\right] = \lim_{\mathrm{T}\to 0}\left[\frac{\bar{n}}{T}mT\right] = \bar{n}m = -\frac{9\pi}{16}\frac{\Gamma}{D_{32}^2}\bar{n} \tag{41}$$

The time change in the volumetric fraction $\bar{\alpha}^D$ (see Equation (11)) is calculated by using the results represented by Equations (33) and (41):

$$\frac{\mathrm{d}\bar{\alpha}^D}{\mathrm{d}t} = \frac{\pi}{6}E(D_\mathrm{p}^3)\frac{\mathrm{d}}{\mathrm{d}t}\bar{n} + \bar{n}\frac{\pi}{6}\frac{\mathrm{d}}{\mathrm{d}t}E(D_\mathrm{p}^3)$$

$$= -\frac{\pi}{6}\frac{16}{9\pi}D_{32}^3\cdot\frac{9\pi}{16}\frac{\Gamma}{D_{32}^2}\bar{n} - \bar{n}\frac{\pi}{6}\cdot\frac{3}{2}\Gamma D_{32} = -\frac{45}{32}\pi\frac{\Gamma\bar{\alpha}^D}{D_{32}^2} \tag{42}$$

The time change of the Sauter mean diameter (Equation (28)) consists of the deviations of the volumetric fraction and the surface fraction:

$$\dot{D}_{32} = \frac{6}{\bar{a}^2}\left(\bar{a}\frac{\mathrm{d}\bar{\alpha}^D}{\mathrm{d}t} - \bar{\alpha}^D\frac{\mathrm{d}\bar{a}}{\mathrm{d}t}\right) = D_{32}\left(\frac{1}{\bar{\alpha}^D}\frac{\mathrm{d}\bar{\alpha}^D}{\mathrm{d}t} - \frac{1}{\bar{a}}\frac{\mathrm{d}\bar{a}}{\mathrm{d}t}\right) \tag{43}$$

Utilizing the results following from Equations (32) and (42), the change in the surface fraction can also be formulated in terms of the evaporation constant and the Sauter mean diameter:

$$\frac{1}{\bar{a}}\frac{\mathrm{d}\bar{a}}{\mathrm{d}t} = \frac{1}{\bar{\alpha}^D}\frac{\mathrm{d}\bar{\alpha}^D}{\mathrm{d}t} - \frac{1}{D_{32}}\frac{\mathrm{d}D_{32}}{\mathrm{d}t} = -\frac{9\pi}{8}\frac{\Gamma}{D_{32}^2} \quad \Rightarrow \quad \frac{\mathrm{d}\bar{a}}{\mathrm{d}t} = -\frac{9\pi}{8}\frac{\Gamma}{D_{32}^2}\bar{a} \tag{44}$$

The source terms of the α-equation (Equation (42)) and the a-equation (Equation (44)) stay in the following relationship:

$$\frac{1}{\bar{\alpha}^D}\frac{\mathrm{d}\bar{\alpha}^D}{\mathrm{d}t} = \frac{5}{4}\cdot\frac{1}{\bar{a}}\frac{\mathrm{d}\bar{a}}{\mathrm{d}t} \tag{45}$$

Obviously, the source terms in both transport equations can be formulated in terms of the same parameter: τ_Γ (Equation (48)). With the definition of the particle diameter PDF as the starting point, the evaporation process is finally modelled by the following two transport equations:

$$\partial_t(\rho^D\bar{\alpha}^D) + \partial_j(\rho^D\bar{\alpha}^D\langle u_j^D\rangle^D) = -\tfrac{5}{4}\rho^D\tau_\Gamma^{-1}\bar{\alpha}^D \tag{46}$$

$$\partial_t(\rho^D\bar{a}) + \partial_j(\rho^D\bar{a}\langle u_j^D\rangle^D) = -\rho^D\tau_\Gamma^{-1}\bar{a} \tag{47}$$

DOI: 10.1002/fld

The convective transport in both equations is defined by the volume-fraction-weighted averaged particle velocity $\langle u_i^D \rangle^D$ [33]. The first equation (Equation (46)) originates from the well-known mass balance of the dispersed phase with a mass transfer defining source term. The second equation (Equation (47)) governs the surface fraction of the dispersed phase, being the synonym for the cloud surface per volume. The evaporation time scale τ_Γ, the source terms of this evaporation-describing two-equation model depend upon, reads

$$\tau_\Gamma = -\bar{a}\left(\frac{\mathrm{d}\bar{a}}{\mathrm{d}t}\right)^{-1} = \frac{8}{9\pi}\frac{D_{32}^2}{\Gamma} \tag{48}$$

Accordingly, the transport of both quantities α^D and a depends on the evaporation constant Γ, which is given by the d^2-law. Introducing the definition of the evaporation constant, the final expression serving for the determination of the evaporation time scale is given by

$$\tau_\Gamma = \frac{D_{32}^2}{12}\frac{\rho^D}{\rho^C}[D_{\alpha\beta} Sh^* \ln(1+B_\mathrm{M})]^{-1} \tag{49}$$

By solving the equations of the α–a-model the evaporation rate of a spray stream can be quantified. In such a manner, the mass balance of a two-phase flow is completely satisfied.

2.6. Vapor transfer

The gaseous phase was considered as a two-component mixture consisted of dry air and vapor. The equation governing the vapor mass ratio Y $(=\rho^{\mathrm{vapor}}/\rho^C)$ of a humid gas reads

$$\partial_t(\rho^C Y) + \partial_j(\rho^C Y u_j^C) = \partial_j(\rho^C D_{\alpha\beta}\partial_j Y) \tag{50}$$

with the binary diffusion coefficient $D_{\alpha\beta}$ taking the following form [36]:

$$D_{\alpha\beta} = \frac{(1013\times 10^5\,\mathrm{Pa}/p)T^{7/4}\times 10^{-3/2}((M^{\mathrm{air}}+M^{\mathrm{vapor}})/M^{\mathrm{air}}\cdot M^{\mathrm{vapor}})^{1/2}}{[(\sum_\alpha v_\alpha^{\mathrm{air}})^{1/3}+(\sum_\alpha v_\alpha^{\mathrm{vapor}})^{1/3}]^2}$$
$$\times 10^{-12}\left(\frac{\mathrm{kg}}{\mathrm{mol}}\right)^{1/2}\mathrm{K}^{-7/4}\frac{\mathrm{m}^2}{\mathrm{s}} \tag{51}$$

$$\sum_\alpha v_\alpha^{\mathrm{air}} = 20,1, \quad \sum_\alpha v_\alpha^{\mathrm{water}} = 12,7 \tag{52}$$

The diffusion-like turbulent transport of the vapor mass ratio (originating from the averaging of its convective transport) is modelled by utilizing the simple gradient diffusion hypothesis with the coefficient being the function of the turbulent Schmidt number Sc_t:

$$\langle u_j^C Y'\rangle^C = -\frac{\nu_t^C}{Sc_t}\partial_j\bar{Y}, \quad Sc_t = 0,85 \tag{53}$$

$$\partial_t(\rho^C\bar{\alpha}^C\bar{Y}) + \partial_j(\rho^C\bar{\alpha}^C\langle u_j^C\rangle^C\bar{Y})$$
$$= \partial_j\left[\rho^C\bar{\alpha}^C\left(D_{\alpha\beta}+\frac{\nu_t^C}{Sc_t}\right)\partial_j\bar{Y}\right] + \frac{5}{4}\frac{\rho^D}{\tau_\Gamma}\bar{\alpha}^D \tag{54}$$

DOI: 10.1002/fld

The mass transfer rate (Equation (49); see also Equation (46)) features the additional source term in this transport equation. The density of the continuous phase, consisting of fluid vapor and air ($\rho^C = \rho^{\text{air}} + \rho^{\text{vapor}}$), is defined by the sum of their partial densities. The partial density of vapor arises from the definition of the vapor mass ratio Y:

$$Y = \frac{\rho^{\text{vapor}}}{\rho^{\text{air}} + \rho^{\text{vapor}}} = \left(\frac{\rho^{\text{air}}}{\rho^{\text{vapor}}} + 1 \right)^{-1} \Rightarrow \rho^C = \frac{\rho^{\text{vapor}}}{Y} = \frac{\rho^{\text{air}}}{1-Y} \tag{55}$$

The partial density of air

$$\rho^{\text{air}} = x^{\text{air}} \frac{M^{\text{air}}}{R_0 T^C} p \tag{56}$$

follows from the definition of the partial density of vapor and the volumetric air fraction x^{air}:

$$\rho^{\text{air}} \frac{Y}{1-Y} = \rho^{\text{vapor}} = (1 - x^{\text{air}}) \frac{M^{\text{vapor}}}{R_0 T^C} p \tag{57}$$

$$\Rightarrow x^{\text{air}} = \left(1 + \frac{Y}{1-Y} \frac{M^{\text{air}}}{M^{\text{vapor}}} \right)^{-1} \tag{58}$$

By introducing the expression for the partial density of air (Equation (56)) into Equation (55), the density of the continuous phase is formulated as follows:

$$\rho^C = (1-Y)^{-1} \left(1 + \frac{Y}{1-Y} \frac{M^{\text{air}}}{M^{\text{vapor}}} \right)^{-1} \frac{M^{\text{air}}}{R_0 T^C} \tag{59}$$

With the last expression, the transport equation of the vapor mass ratio (Equation (54)) is closed.

2.7. Heat transfer

The heat transfer across the surface of an evaporating drop has to be solved simultaneously with the mass exchange between the phases. The proper description of the thermodynamics of a two-phase flow requests the molecular processes and the variable flow properties to be accounted for. The mixing of vapor and air causes a substantial change of the Mol mass and specific heat of the continuous phase as follows:

$$\frac{1}{M^C} = \frac{1-Y}{M^{\text{air}}} + \frac{Y}{M^{\text{vapor}}}, \quad c_{\text{p}}^C = (1-Y) c_{\text{p}}^{\text{air}} + Y c_{\text{p}}^{\text{vapor}} \tag{60}$$

Based on the theory of the ideal gases with $c_\omega^{\text{id}} = c_{\text{p}}^C - R_0 / M^C$, the conductivity of the continuous phase is defined by the following model [36]:

$$\lambda^C = \mu^C \left(1,3 c_\omega^{\text{id}} + 1,762 \frac{R_0}{M^C} - 0,352 \frac{R_0}{M^C} \frac{T_{\text{crit}}^{\text{air}}}{T^C} \right) \tag{61}$$

$$T_{\text{crit}}^{\text{air}} = 133,2\,\text{K}, \quad M^{\text{air}} \approx 0,029 \frac{\text{kg}}{\text{mol}} \tag{62}$$

The radiative heat flux per volume $\dot{q}_{\text{rad}}^D$, absorbed by a particle, is defined in terms of its surface area per volume a, the absorption coefficient of the dispersed phase $\varepsilon_{\text{abs}}^D$ and the difference of the

DOI: 10.1002/fld

fourth powers of the absolute temperatures

$$\dot{q}^D_{\mathrm{rad}} = a\varepsilon^D_{\mathrm{abs}}\sigma[(T^C)^4 - (T^D)^4], \quad \varepsilon^D_{\mathrm{abs}} = \varepsilon^{\mathrm{water}}_{\mathrm{abs}} = 0,92 \tag{63}$$

with the Stephan–Boltzmann constant $\sigma = 5,67051 \times 10^{-8}\,\mathrm{W/(m^2K)}$. This term represents an additional source term in the equation of thermal transport. Owing to the equivalence of emission and absorption coefficients, the radiative flux can take negative values, if the dispersed phase is on the a higher temperature level compared with the continuous one.

As defined in the evaporation model of Abramzon and Sirignano [22], the heat transfer at the surface of an evaporating drop depends on the latent heat $L(T^D)$, the temperature difference and the mass transfer $\dot{m}$:

$$Q_{\mathrm{L}} = \dot{m}\left[\frac{c^D_{\mathrm{p}}(T^C - T^D)}{B_{\mathrm{T}}} - L(T^D)\right] \tag{64}$$

The heat transfer coefficient B_{T} is to be computed from the Abramson and Sirignano model algorithm, see Section 3. By utilizing Equation (46), this heat source term can be expressed in terms of τ_Γ in a volume-specific manner.

Using the following definition of the evaporation enthalpy [37],

$$\Delta h_v = \frac{R_0}{M^{\mathrm{vapor}}}\left(\frac{1}{T^D} - \frac{1}{T_{\mathrm{ref}}}\right)^{-1} \ln\frac{p_{\mathrm{sat}}(T_{\mathrm{ref}})}{p_{\mathrm{sat}}(T^D)} \tag{65}$$

the heat, which is used for the evaporation process, can be subtracted from the heat of the continuous phase. The temperature T_{ref} denoting the gas temperature near the drop surface is formulated by the $\frac{1}{3}$-law [38]:

$$T_{\mathrm{ref}} = T^D + A_r(T^C - T^D) \quad \text{with } A_r = \tfrac{1}{3} \tag{66}$$

In analogy to the mass transfer, the turbulent diffusion of the heat of both phases is modelled by simple gradient diffusion hypothesis in terms of turbulent Prandtl number Pr^k_t.

$$\langle u^k_i T'^k\rangle^k = -\frac{\nu^k_t}{Pr^k_t}\partial_i \bar{T}^k; \quad Pr^C_t = 0,6; \quad Pr^D_t = 1,0 \tag{67}$$

The final two equations completing the Euler/Euler computational scheme are those governing the thermal transport between the phases being represented by the particular set of temperature equations. These equations originate from the enthalpy transport. Although the deviation of air enthalpy $\mathrm{d}h^C$ is proportional to its temperature, the deviation of water enthalpy $\mathrm{d}h^D$ is proportional to the temperature difference with reference to the melting point temperature $T^D_0 = 273,15\,\mathrm{K}$. The radiation emitted by the gas i.e. absorbed by liquid phase $\dot{q}_{\mathrm{rad}}$, evaporation heat (represented by the evaporation enthalpy Δh_v), latent heat $L(T^D)$, molecular and turbulent conduction as well as the conduction at the boundaries between the phases are herewith accounted for:

$$\begin{aligned}&\partial_t(\rho^C\bar{\alpha}^C\bar{T}^C) + \partial_j(\rho^C\bar{\alpha}^C\langle u^C_j\rangle^C\bar{T}^C)\\ &\quad = \partial_j\left[\bar{\alpha}^C\left(\frac{\lambda^C}{c^C_{\mathrm{p}}} + \rho^C\frac{\nu^C_t}{Pr^C_t}\right)\partial_j\bar{T}^C\right] - \frac{\overline{\dot{q}_{\mathrm{rad}}}}{c^C_{\mathrm{p}}} + \frac{5}{4}\rho^D\frac{\bar{\alpha}^D}{\tau_\Gamma}\frac{c^D_{\mathrm{p}}}{c^C_{\mathrm{p}}}\left[\frac{\bar{T}^D - \bar{T}^C}{B_{\mathrm{T}}} + \frac{L(T^D)}{c^D_{\mathrm{p}}} - \frac{\Delta h_v}{c^D_{\mathrm{p}}}\right]\end{aligned} \tag{68}$$

DOI: 10.1002/fld

$$\partial_t[\rho^D\bar{\alpha}^D(\bar{T}^D-T_0^D)]+\partial_j[\rho^D\bar{\alpha}^D\langle u_j^D\rangle^D(\bar{T}^D-T_0^D)]$$
$$=\partial_j\left(\bar{\alpha}^D\rho^D\frac{v_t^D}{Pr_t^D}\partial_j\bar{T}^D\right)+\frac{\overline{\dot{q}_{\mathrm{rad}}}}{c_{\mathrm{p}}^D}-\frac{5}{4}\rho^D\frac{\bar{\alpha}^D}{\tau_\Gamma}\left[\frac{\bar{T}^D-\bar{T}^C}{B_{\mathrm{T}}}+\frac{L(T^D)}{c_{\mathrm{p}}^D}\right] \tag{69}$$

2.8. Turbulence modelling

The background turbulence model for both phases is based on the Boussinesq analogy employing eddy viscosity μ_t^k (Equation (19)) as the model quantity. The turbulence of the dispersed liquid phase is characterized by its turbulence kinetic energy (Equation (9)) and the covariance of velocities of the particulate liquid phase and carrier gas phase $q=\langle\{u_i^D\}^D\{u_i^C\}^C\rangle^D$ in line with the proposal by He and Simonin [8], for which the transport equations

$$\rho^D\bar{\alpha}^D\partial_t k^D+\rho^D\bar{\alpha}^D\langle u_j^D\rangle^D\partial_j k^D$$
$$=\frac{\rho^D\bar{\alpha}^D}{\tau_{\mathrm{p}}}(q-2k^D)-\rho^D\bar{\alpha}^D\langle\{u_i^D\}^D\{u_j^D\}^D\rangle^D\partial_j\langle u_i^D\rangle^D$$
$$+\partial_j(K_t^D\bar{\alpha}^D\partial_j k^D)-\rho^D\bar{\alpha}^D\varepsilon_{\mathrm{c}}^D \tag{70}$$

$$\rho^D\bar{\alpha}^D\partial_t q+\rho^D\bar{\alpha}^D\langle u_j^D\rangle^D\partial_j q$$
$$=\frac{\rho^D\bar{\alpha}^D}{\tau_{\mathrm{p}}}(2Zk^D+2k^C-(1+Z)q)-\rho^D\bar{\alpha}^D\langle\{u_i^D\}^D\{u_j^C\}^C\rangle^D\partial_j\langle u_i^C\rangle^C$$
$$-\rho^C\bar{\alpha}^C\langle\{u_i^C\}^C\{u_j^D\}^D\rangle^D\partial_j\langle u_i^D\rangle^D$$
$$+\partial\left(\rho^D\bar{\alpha}^D\frac{\nu_\alpha}{\sigma_k}\partial_j q\right)-\rho^D\bar{\alpha}^D\frac{q}{\tau_\alpha}+\frac{5}{4}\rho^D\frac{\bar{\alpha}^D}{\tau_\Gamma}(k^C+k^D) \tag{71}$$

with the mass loading $Z=\rho^D\alpha^D/(\rho^C\alpha^C)$, are to be solved. The diffusion coefficients v_t^D and K_t^D are modified to account for the influence of drop collisions on the disperse phase turbulence, Jenkins and Richman [16]:

$$v_t^D=\left(\nu_\alpha+\frac{1}{3}\tau_{\mathrm{p}}k^D\right)\left(1+\frac{1}{2}\tau_{\mathrm{p}}\frac{\sigma_{\mathrm{c}}}{\tau_{\mathrm{c}}}\right)^{-1}\quad\text{with }\sigma_{\mathrm{c}}=(1+e_{\mathrm{c}})(3-e_{\mathrm{c}})/5 \tag{72}$$

$$K_t^D=\left(\frac{\nu_\alpha}{\sigma_k}+\frac{5}{9}\tau_{\mathrm{p}}\frac{2}{3}k^D\right)\left(1+\frac{5}{9}\tau_{\mathrm{p}}\frac{\xi_{\mathrm{c}}}{\tau_{\mathrm{c}}}\right)^{-1}\quad\text{with }\xi_{\mathrm{c}}=(1+e_{\mathrm{c}})(49-33e_{\mathrm{c}})/100 \tag{73}$$

$$v_n^a=-e_{\mathrm{c}}\cdot v_n^b,\quad \varepsilon_{\mathrm{c}}^D=\frac{1-e_{\mathrm{c}}^2}{\tau_{\mathrm{c}}}\cdot\frac{2}{3}k^D \tag{74}$$

The collision-dependent dissipation rate $\varepsilon_{\mathrm{c}}^D$, mimicking inelastic bouncing of the droplets, accounts for reduction in the turbulence intensity of the disperse phase. The parameter e_{c} is defined by ratio of the normal rebound velocity v_n^a to the normal impact velocity v_n^b. In the case of inelastic

DOI: 10.1002/fld

particle bouncing ($0 \leqslant e_c < 1$), the dissipation rate ε_c^D is positive, whereas it takes the value zero if elastic bouncing ($e_c = 1$) occurs.

The turbulence of the continuous phase is modelled by an extended $k-\varepsilon$ model, which consists of the transport equations of the turbulent kinetic energy

$$\begin{aligned}
&\rho^C \bar{\alpha}^C \partial_t k^C + \rho^C \bar{\alpha}^C \langle u_j^C \rangle^C \partial_j k^C \\
&\quad = \rho^D \bar{\alpha}^D \left(\frac{1}{\tau_p} + \frac{5}{4} \frac{1}{\tau_\Gamma} \right) (q - 2k^C) - \rho^C \bar{\alpha}^C \langle \{u_i^C\}^C \{u_j^C\}^C \rangle^C \partial_j \langle u_i^C \rangle^C \\
&\quad + \partial_j \left[\left(\mu^C + \frac{\mu_t^C}{\sigma_k} \right) \bar{\alpha}^C \partial_j k^C \right] - \rho^C \bar{\alpha}^C \varepsilon_M^C
\end{aligned} \tag{75}$$

and its dissipation rate

$$\begin{aligned}
&\rho^C \bar{\alpha}^C \partial_t \varepsilon_M^C + \rho^C \bar{\alpha}^C \langle u_j^C \rangle^C \partial_j \varepsilon_M^C \\
&\quad = \rho^D \bar{\alpha}^D \left(\frac{5}{4} \frac{1}{\tau_\Gamma} + \frac{C_{\varepsilon 3}}{\tau_p} \right) \varepsilon_M^C \left(\frac{q}{k^C} - 2 \right) - C_{\varepsilon 1} \rho^C \bar{\alpha}^C \frac{\varepsilon_M^C}{k^C} \langle \{u_i^C\}^C \{u_j^C\}^C \rangle^C \partial_j \langle u_i^C \rangle^C \\
&\quad + \partial_j \left[\left(\mu^C + \frac{\mu_t^C}{\sigma_\varepsilon} \right) \bar{\alpha}^C \partial_j \varepsilon_M^C \right] - C_{\varepsilon 2} \rho^C \bar{\alpha}^C \frac{\varepsilon_M^{C2}}{k^C}
\end{aligned} \tag{76}$$

with the constants $C_{\varepsilon 1} = 1,44$, $C_{\varepsilon 2} = 1,92$ and $C_{\varepsilon 3} = 1,2$ and the Prandtl–Schmidt numbers $\sigma_k = 1.0$ and $\sigma_\varepsilon = 1.3$. Note the dependency on the evaporation time scale τ_Γ (Equation (49)) in the source terms of the last three transport equations. The additional source terms in the equations of the continuous phase show that evaporation rate written in terms of the evaporation time scale τ_Γ exhibits similar effects on the turbulence as the drag forces, modelled in terms of the relaxation time scale τ_p. It should be noted here that due to the evaporation of the dispersed phase (the mass transport is present only in one direction: from disperse to the continuous phase) the influence of the mass transfer rate is restricted to the volumetric fraction of the dispersed phase only and has no influence on its turbulent kinetic energy (Equation (70)).

3. EVAPORATION MODELLING

The liquid mass leaving the droplet in the evaporation process influences strongly both the heat and mass transfer between the phases. This process is accounted for by the Spalding heat and mass transfer coefficients B_T (Equation (64)) and B_M (Equation (48)). This section outlines the algorithm for their determination. As pointed out previously, the evaporation model proposed by Abramzon and Sirignano [22] was adopted here as the background model. In the framework of their model, the above-mentioned coefficients as well as the modified Nusselt Nu^* and Sherwood numbers Sh^* are defined in terms of the relative humidity of the continuous phase.

3.1. Saturation pressure and relative humidity

During the evaporation process, the humidity in the air and the vapor mass ratio increase until the partial pressure has reached the saturation pressure (Figure 2). Based on the following functional

DOI: 10.1002/fld

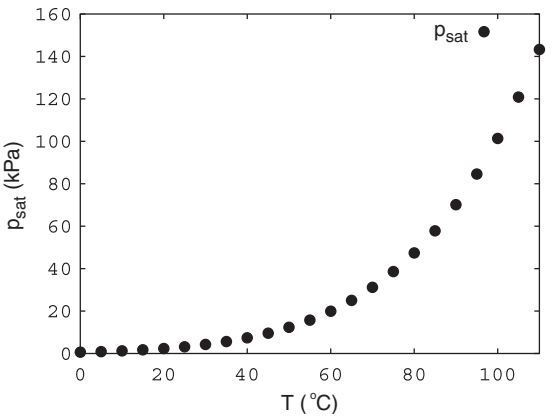

Figure 2. Temperature-dependent saturation pressure of water vapor.

dependency between the maximum vapor mass ratio Y_{sat}, the absolute pressure p and the saturation pressure p_{sat} [39]

$$Y_{\text{sat}} = (1 - Y_{\text{sat}}) 0,622 \frac{p_{\text{sat}}}{p - p_{\text{sat}}} \tag{77}$$

the maximum vapor mass ratio and the relative humidity can be determined:

$$\Rightarrow\ Y_{\text{sat}} = \frac{0,622}{p - p_{\text{sat}}/p_{\text{sat}} + 0,622} = \frac{0,622 p_{\text{sat}}}{p - 0,378 p_{\text{sat}}} \tag{78}$$

The relative humidity $0 \leqslant \phi \leqslant 1$ is defined by the ratio of the vapor mass ratio to its maximum: $\phi (= \rho^{\text{vapor}} / \rho_{\text{sat}}^{\text{vapor}}) = Y / Y_{\text{sat}}$.

3.2. Heat-transfer-dependent mass transfer

The mass transfer per surface of a cloud of spherical particles

$$\begin{aligned} \frac{\dot{m}}{A_O} &= \rho^C D_{\alpha\beta} B_{\text{M}} \frac{Sh}{E(D_{\text{p}})} \quad \text{with } A_O = \pi E(D_{\text{p}}^2) \\ \Rightarrow\ \dot{m} &= \rho^C \pi D_{21} D_{\alpha\beta} Sh B_{\text{M}} \end{aligned} \tag{79}$$

depends on the Sherwood Number Sh and the mass transfer coefficient B_{M}:

$$\begin{aligned} B_{\text{M}} &= \frac{Y_{\text{sat}} - Y_\infty}{1 - Y_{\text{sat}}} = \frac{Y_{\text{sat}}}{1 - Y_{\text{sat}}} - \frac{Y_\infty}{1 - Y_{\text{sat}}} \\ &= \frac{0,622 p_{\text{sat}} - Y_\infty (p - 0,378 p_{\text{sat}})}{p - p_{\text{sat}}} \end{aligned} \tag{80}$$

DOI: 10.1002/fld

The heat flux

$$Q_{\mathrm{L}} = Nu\pi D_{21}\lambda^{C}(T^{C}-T^{D}) - \dot{m}L(T^{D}) \tag{81}$$

depending on the Nusselt number Nu can also be defined in terms of the heat transfer coefficient B_{T} and the liquid temperature-dependent latent heat $L(T^{D})$:

$$B_{\mathrm{T}} = \frac{c_{\mathrm{p}}^{D}(T^{C}-T^{D})}{Q_{\mathrm{L}}/\dot{m}+L(T^{D})} \Rightarrow Q_{\mathrm{L}} = \dot{m}\left(\frac{c_{\mathrm{p}}^{D}(T^{C}-T^{D})}{B_{\mathrm{T}}} - L(T^{D})\right) \tag{82}$$

Utilizing the heat flux definition given by Equation (81), the mass transfer rate formulae can be finally written as a function of the Nusselt number

$$\dot{m} = \pi D_{21}\frac{\lambda^{C}}{c_{\mathrm{p}}^{D}} Nu\, B_{\mathrm{T}} \tag{83}$$

In such a manner, the mass transfer from the liquid to the gas phase can be determined. Here, the Nusselt number is calculated using the algorithm outlined in the following subsection.

3.3. Evaporation algorithm

Starting from the initial values of Nusselt and Sherwood numbers

$$Nu_{0} = 1 + (1 + Re_{\mathrm{rel}}\, Pr)^{1/3} \cdot f(Re_{\mathrm{rel}}) \tag{84}$$

$$Sh_{0} = 1 + (1 + Re_{\mathrm{rel}}\, Sc)^{1/3} \cdot f(Re_{\mathrm{rel}}) \tag{85}$$

with

$$f(Re_{\mathrm{rel}}) = \begin{vmatrix} 1, & Re_{\mathrm{rel}} \leqslant 1 \\ Re_{\mathrm{rel}}^{0{,}077}, & \text{else} \end{vmatrix} \tag{86}$$

and

$$Pr = \frac{c_{\mathrm{p}}^{C}\mu^{C}}{\lambda^{C}}, \quad Sc = \frac{\mu^{C}}{\rho^{C} D_{\alpha\beta}}$$

(see Equation (14) for the definition of Re_{rel}) the modifications according to Abramzon and Sirignano [22] are defined in the following manner:

$$2 + \frac{Sh_{0}-2}{F(B_{\mathrm{M}})} = Sh^{*} = Sh\,\frac{B_{\mathrm{M}}}{\ln(1+B_{\mathrm{M}})} \tag{87}$$

$$2 + \frac{Nu_{0}-2}{F(B_{\mathrm{T}})} = Nu^{*} = Nu\,\frac{B_{\mathrm{T}}}{\ln(1+B_{\mathrm{T}})} \tag{88}$$

with

$$F(B) = (1+B)^{0{,}7}\frac{\ln(1+B)}{B} \quad \text{and} \quad \mathrm{Le} = \frac{Sc}{Pr} = \frac{\lambda^{C}}{\rho^{C} c_{\mathrm{p}}^{C} D_{\alpha\beta}}$$

DOI: 10.1002/fld

Introducing these modified Sherwood and Nusselt numbers into the mass transfer equations (79) and (83)

$$\dot{m} = \pi D_{21} \frac{\lambda^C}{c_p^D} Nu^* \ln(1+B_T), \quad \dot{m} = \pi D_{21} \rho^C D_{\alpha\beta} Sh^* \ln(1+B_M) \tag{89}$$

$$\Rightarrow \frac{c_p^C}{c_p^D} \underbrace{\frac{\lambda^C}{\rho^C c_p^C D_{\alpha\beta}}}_{=\mathrm{Le}} Nu^* \ln(1+B_T) = Sh^* \ln(1+B_M) \tag{90}$$

the exponent ϕ_B featuring in the heat transfer coefficient equation

$$B_T = (1+B_M)^{\phi_B} - 1$$

is solved by the following formulation arising from Equation (89)

$$\phi_B = \frac{\ln(1+B_T)}{\ln(1+B_M)} = \frac{c_p^D}{c_p^C} \frac{Sh^*}{Nu^*} \mathrm{Le}^{-1} \tag{91}$$

Using this definition and the initial condition $Nu^{*(0)} = Nu_0$, the following iterative algorithm is used for the Nusselt number determination:

$$\phi_B^{(n)} = \frac{c_p^D}{c_p^C} \frac{Sh^*}{Nu^{*(n)}} \mathrm{Le}^{-1} \tag{92}$$

$$B_T^{(n+1)} = (1+B_M)^{\phi_B^{(n)}} - 1, \quad Nu^{*(n+1)} = 2 + \frac{Nu_0 - 2}{F(B_T^{(n+1)})} \tag{93}$$

The truncation condition is defined by the ratio of the heat transfer coefficients:

$$\left| \frac{B_T^{(n+1)}}{B_T^{(n)}} - 1 \right| < \varepsilon$$

Herewith, the computational scheme describing the processes of the heat and mass transfer in an evaporating two-phase flow is completed.

4. NUMERICAL METHOD

The Euler/Euler computations were performed with an in-house computer code FAN3D based on a finite volume numerical method for solving three-dimensional RANS equations on block-structured, body-fitted, non-orthogonal meshes. Block interfaces are treated in a conservative manner, consistent with the treatment of inner cell faces. Cell-centered (collocated) variable arrangement and cartesian vector and tensor components are used. The equations are linearized and solved sequentially using an iterative ILU method. The well-known SIMPLE algorithm, modified to account for volumetric fraction, was applied for coupling the velocity and pressure fields in the transport equation governing the momentum of the continuous phase enabling in such a manner fulfillment of the continuity condition. Unfortunately, a similar algorithm does not exist for the discrete

DOI: 10.1002/fld

phase, leading eventually to convergence problems, particularly in regions where the fraction of discrete particles is either zero or very close to zero (e.g. in the corner behind a backward-facing step). The convective transport of the volumetric fraction of the disperse phase α^D is approximated by blending an upwind discretization scheme (UDS), modified to account properly for the influence of the void fraction gradients on the weighted fluxes, and central differencing (see [40] for further details), whose stability was enhanced through the so-called deferred correction approach.

When using the standard UDS a simplified one-dimensional simulation of a flow from 'west' to 'east' would imply the transport equation for the volume fraction discretized by the following system of algebraic equations ($\mathbf{L}\boldsymbol{\alpha}=\mathbf{b}$):

$$\begin{pmatrix} a_1 & & & & \\ -a_2 & a_2 & & & \\ & -a_3 & a_3 & & \\ & & \ddots & \ddots & \\ & & & -a_n & a_n \end{pmatrix} \begin{pmatrix} \alpha_1^D \\ \alpha_2^D \\ \alpha_3^D \\ \vdots \\ \alpha_n^D \end{pmatrix} = \begin{pmatrix} f_0^c \alpha_0^D A_0 \\ 0 \\ 0 \\ \vdots \\ 0 \end{pmatrix} \quad \text{with } a_i = f_{i-1}^c A_{i-1}, \quad i \in \{1, \ldots, n\} \tag{94}$$

where $f_0^c \alpha_0^D$ represents the mass flux of the dispersed phase over the grid-cell inlet surface A_0. Physically, if the particles would accelerate (e.g. due to gravity forces), the number density and the volumetric fraction would decrease. However, by applying the standard upwind discretization procedure the volumetric fraction α^D would remain constant, independent of the velocity field:

$$\alpha_1^D = \alpha_0^D \tag{95}$$

$$\alpha_i^D = \alpha_{i-1}^D \quad \text{for } i \in \{2, \ldots, n\} \tag{96}$$

$$\Rightarrow \alpha_i^D = \alpha_0^D \quad \text{for } i \in \{1, \ldots, n\} \tag{97}$$

In order to fulfill the conservativeness, the difference between velocities on the 'east' and 'west' side of the computational cell has to be accounted for. Accordingly, the diagonal elements of the coefficient matrix have to be appropriately modified to simulate the accelerating flow:

$$a_P = \max(f_e^c; 0) + \max(-f_w^c; 0) \tag{98}$$

In addition to the matrix L_{ij} used within the standard upwind discretization (Equation (94)), the modified matrix $(\mathbf{L}+\mathbf{M})\boldsymbol{\alpha}=\mathbf{b}$ contains an additional term:

$$M_{ij} = \delta_{ij}(A_e \max(f_e^c; 0) + A_w \max(-f_w^c; 0)$$

$$-A_e \max(-f_e^c; 0) - A_w \max(f_w^c; 0)) = \delta_{ij}(f_e^c A_e - f_w^c A_w) \tag{99}$$

DOI: 10.1002/fld

providing the conservativeness condition to be satisfied when computing the accelerating and decelerating flows. The modified system of algebraic equations now takes the following form:

$$\begin{pmatrix} a_1 & & & & \\ -a_1 & a_2 & & & \\ & -a_2 & a_3 & & \\ & & \ddots & \ddots & \\ & & & -a_{n-1} & a_n \end{pmatrix} \begin{pmatrix} \alpha_1^D \\ \alpha_2^D \\ \alpha_3^D \\ \vdots \\ \alpha_n^D \end{pmatrix} = \begin{pmatrix} f_0^c \alpha_0^D A_0 \\ 0 \\ 0 \\ \vdots \\ 0 \end{pmatrix} \quad \text{with } a_i = f_i^c A_i, \;\; i \in \{1, \ldots, n\} \tag{100}$$

By using this conservative CUDS, the mass conservation of the dispersed phase is ensured: $f_i^c \alpha_i^D A_i = f_{i-1}^c \alpha_{i-1}^D A_{i-1}; \; i \in \{1, \ldots, n\}$

The convective transport of the carrier phase variables was discretized by an appropriate blended, central differencing scheme. Standard wall functions were applied for modelling the near-wall regions.

4.1. Solution algorithm

Here, the solution algorithm concerning the order of solving of the underlying equations governing the two-phase flow and associated heat and mass transfer is outlined below.

First, the momentum equation (25) governing both the continuous (C) and dispersed (D) phases is to be solved. The corresponding turbulent diffusion coefficients v_t^C and v_t^D are defined in Equations (20) and (72), respectively. The necessary kinetic energy of turbulence k^C, its viscous dissipation rate ε^C, kinetic energy of turbulence k^D (the corresponding turbulent diffusion coefficient K_t^D is given in Equation (73)) and velocity covariance q are to be determined by solving Equations (75), (76), (70) and (71), respectively. The requested relaxation time scale τ_p and collision time scale τ_c are described by Equations (16) and (24). The mass conservation of the continuous phase is described through the well-known pressure correction (p^C) procedure SIMPLE. The continuity of the dispersed phase is described by the equation governing the volume fraction α^D (Equation (46)). Equation (47) defining the transport of the volume-specific phase interface a (surface fraction of the dispersed phase) serves for the determination of the Sauter mean diameter D_{32} (Equation (28)) and appropriate statistical moments (Equation (29)).

The source terms in the continuity, momentum and energy (Equation (68)) equations, being dependent on the mass transfer at the phase interface due to evaporation process, are formulated in terms of the characteristic time scale τ_Γ (Equation (49)). The vapor mass ratio Y and its saturation-pressure-dependent maximum value Y_sat are defined in Equations (54) and (78), respectively. The source terms of the transport equations for temperature of both phases (Equations (68) and (69)) are derived in terms of the continuous phase conductivity λ^C (Equation (61)), the radiative heat flux $\dot{q}_\mathrm{rad}$ (Equation (63)) and the evaporation enthalpy Δh_v (Equation (65)). The heat transfer coefficient B_T (Equation (93)) is to be determined by using the method of Abramson and Sirignano.

Herewith, a system of 12 strongly coupled, partial differential equations for u^C, u^D, p^C, k^C, ε^C, k^D, q, T^C, T^D, Y, α and a describing the two-phase flow under the conditions of phase change due to evaporation process is generated. The equations for T^C, T^D, Y and a are to be omitted when simulating a non-evaporating two-phase flow (as e.g. in Section 5).

DOI: 10.1002/fld

5. COMPUTATIONAL METHOD VERIFICATION AND MODEL VALIDATION

A logical first step in the verification of the computational algorithm presented and the turbulence model validation, before starting the computations of the evaporation process, is to calculate some well-known isothermal, two-phase flow benchmarks for which not only a reference experiment but also a numerical database exist, especially in the Euler–Lagrange framework, whose comparative analysis represents finally the topic of the present study. For this purpose the following two gas–solid flow configurations were chosen: fully developed channel flow (see Figure 3) (e.g. Kulick *et al.* [29]) and flow over a backward-facing step (see Figure 6) representing actually a sudden expansion of the former flow geometry (e.g. Fessler and Eaton [30]). These are the most representative configurations, when dealing with wall-bounded and separated flows. It should be stressed that the background four-equation model has never been tested before in these two cases. It should also be noted that although the flows considered are nominally two-dimensional, the three-dimensional computations accounting for a certain spanwise dimension (the periodic boundary conditions were applied at the side planes) have been performed. For both flows a very extensive and detailed database is available. The interaction between air, representing the continuous phase, and copper, being taken for the monodispersed phase, was investigated in both flow cases. Gravity acts in the positive x-axis direction. The channel flow Reynolds number, based on the channel height ($h=40\,\mathrm{mm}$) and single-phase centerline velocity ($U_0=10.5\,\mathrm{m/s}$), is $Re=27\,600$. The flow is regarded as fully developed after 150 channel heights and at this position it is assumed that the particle velocity and particle turbulence reached an asymptotic state. This fact provided a certain insensibility to the initial conditions. The step height ($H=2h/3=26.7\,\mathrm{mm}$) Reynolds number is $Re=18\,400$. The expansion ratio, representing the ratio of the channel heights after and before expansion, was $ER=(h+H)/h=66.7/40=1.6675$. This value indicates that a fairly intensive perturbation was imposed on the equilibrium channel flow. The ratio of the channel spanwise dimension to the channel height was 11.4, which was considered as sufficient to ensure the flow two dimensionality. The copper particles have a density of $\rho^D=8800\,\mathrm{kg/m^3}$ and a diameter of $D_\mathrm{p}=70\,\mu\mathrm{m}$. The inlet mass loading of particles is $Z_0=10\%$ (the corresponding α^D value can be directly obtained from following formulation: $\alpha^D=\rho^C Z/(\rho^D+\rho^C Z)$) and the parameter of inelasticity is $e_\mathrm{c}=0.9$. The results obtained using the present method were also compared with the computational results obtained by an Euler/Lagrange scheme [31]. In the study of Kohnen, 25 000 particles have been traced through the solution domain within one coupling iteration. Fifteen such iterations were necessary to obtain the converged solution.

5.1. *Particle-laden, fully developed channel flow*

Figures 4 and 5 show the comparison between experimental and numerical results for the streamwise mean velocity and the streamwise and normal-to-the-wall turbulence intensities for both phases.

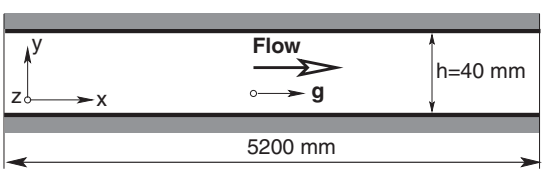

Figure 3. Schematic of the channel flow considered (not to scale).

DOI: 10.1002/fld

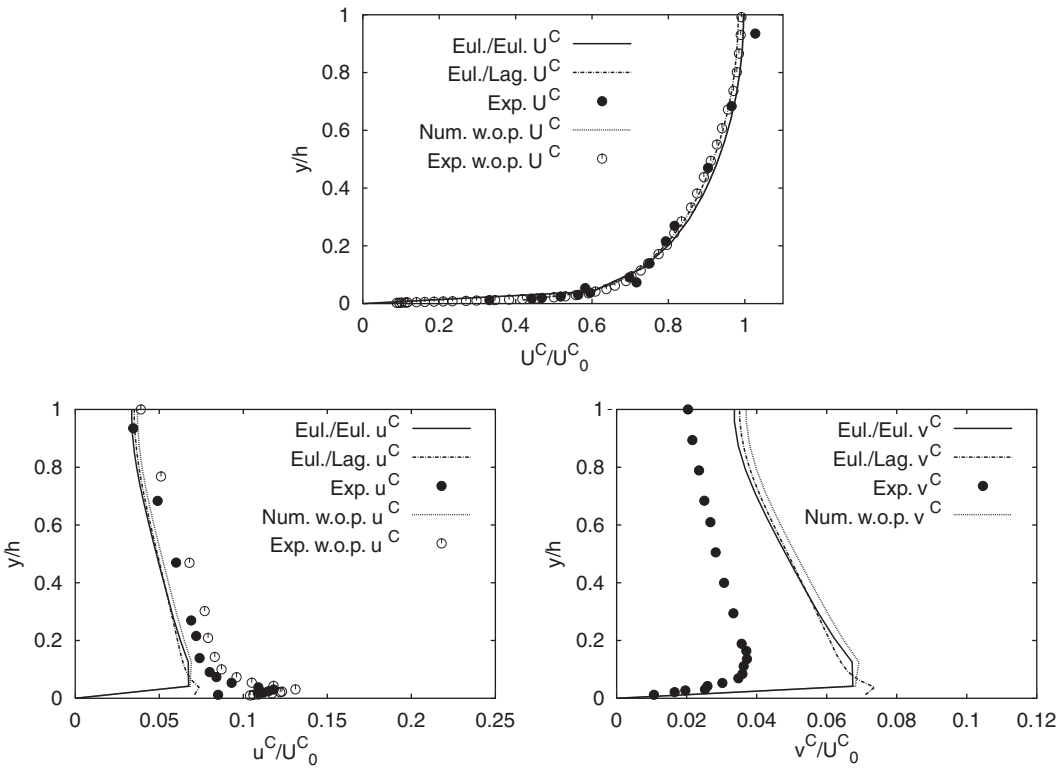

Figure 4. Streamwise mean velocity, streamwise and normal-to-the-wall turbulence intensities of the continuous phase in the fully developed, particle-laden channel flow (w.o.p.—without particles).

For the gaseous phase both sets of results are shown, the results obtained by computing the pure gas flow (unladen flow) and the results of the particle-laden flow. Very good agreement with the experiment is obtained for the streamwise mean velocity component of the gaseous phase, revealing no influence of the particle motion on the gas flow. As expected, the linear eddy viscosity formulation simulating turbulence results in a fully isotropic solution, whereas the experimental results display considerable anisotropy (note different scales for turbulence intensities). The peak level of the streamwise turbulence intensity close to the wall observed in the experiment was not reached in the computation. This discrepancy arises because the equilibrium wall boundary conditions based on the wall function concept were used for modelling the near-wall region. The basic influence of the particles on the gaseous phase is in the attenuation of its turbulence level, as clearly illustrated by the experimental results. This attenuation becomes stronger with increasing wall distance and is more pronounced in the normal-to-the-wall turbulence intensity. This feature is beyond the reach of any eddy viscosity models, either the present model or the Euler/Lagrange method.

The simulated particle velocity (Figure 5) is substantially overpredicted, indicating stronger acceleration of the dispersed phase compared with the experimental observation. Its profile is almost uniform over the entire channel cross-section. The shape of the velocity profile obtained by the Euler/Lagrange method is somewhat closer to the experimental one; however, it is almost

DOI: 10.1002/fld

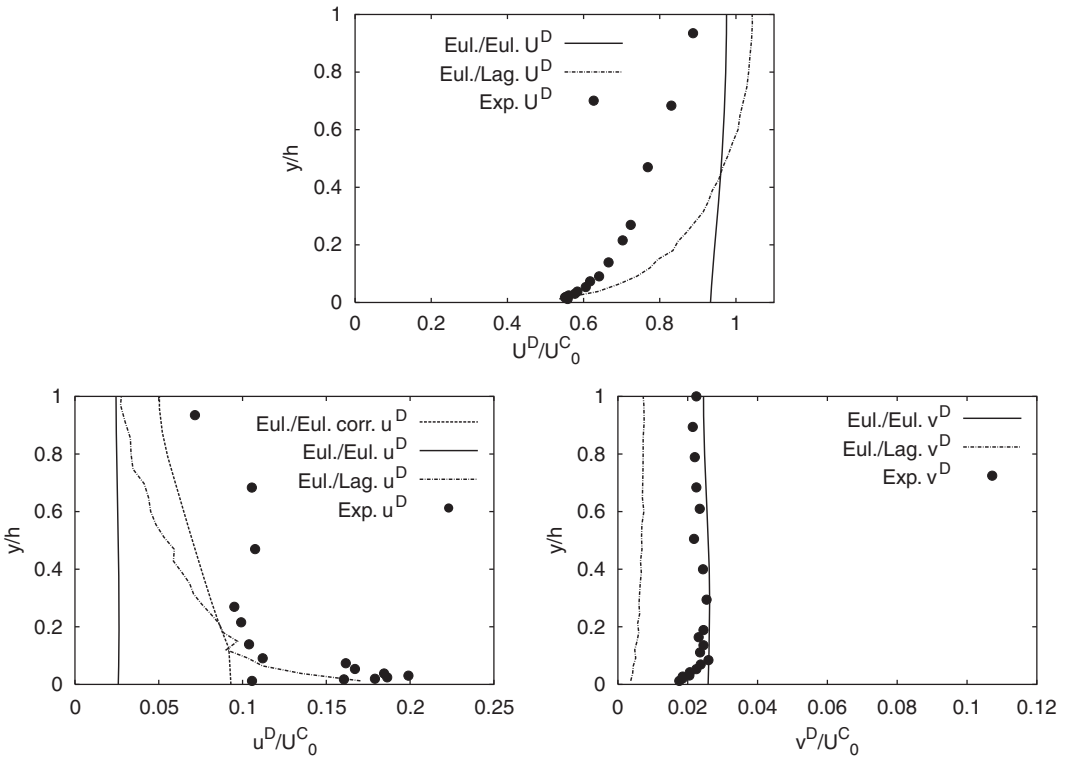

Figure 5. Streamwise mean velocity, streamwise and normal-to-the-wall turbulence intensities of the dispersed phase in the fully developed, particle-laden channel flow.

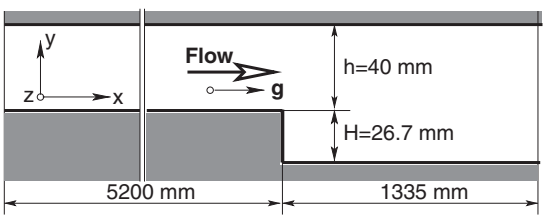

Figure 6. Schematic of the backward-facing step configuration (not to scale).

coincident with the gas velocity profile (see Figure 4 (left)). It seems that in the experiment the particles are slowed down by the gas phase across the entire channel cross-section. Both computational approaches show no capability in reproducing this feature. However, an opposite effect was observed in the experiment of the channel flow behind the step in all characteristic flow zones (compare Figures 7(a) and (b)). The normal-to-the-wall turbulence intensity is strongly underpredicted by the Euler/Lagrange method. Apart from the wall vicinity, reasonable agreement with the experiment was obtained by the present Euler/Euler method, exhibiting only a slight overprediction. The same level was obtained for the streamwise intensity, reflecting again the isotropic solution for the particle phase turbulence. This level is much lower than the experimental results.

DOI: 10.1002/fld

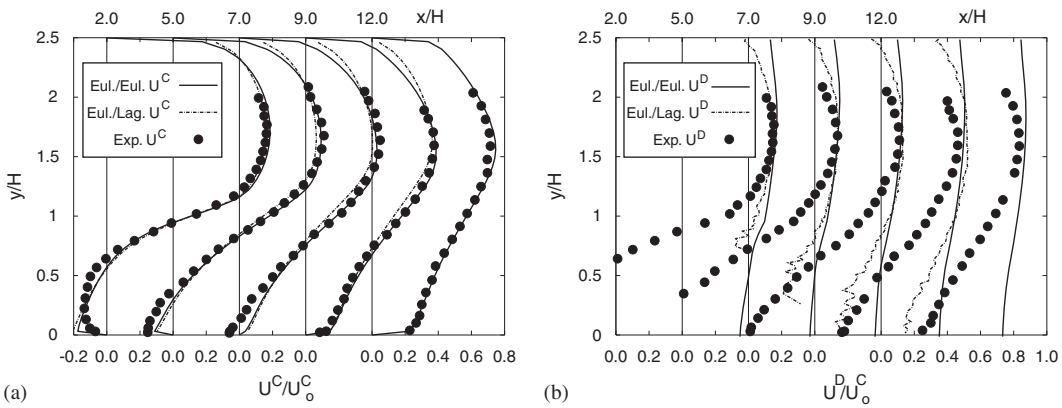

Figure 7. Streamwise velocity component evolution in the particle-laden, backward-facing step flow obtained by both the Euler/Euler and Euler/Lagrange methods: (a) continuous phase (C; gas) and (b) disperse (D; particle) phase.

Issa and Oliveira [41] proposed a kind of 'deferred' correction of the computationally obtained turbulence intensities of the dispersed phase in the framework of their algebraic model. We extended their idea to the differential model used here and applied this procedure to the streamwise turbulence intensity component. The corrected value represents a sum of the gas-phase turbulence intensity and the particle turbulence intensity multiplied by a function of the Stokes number:

$$u^D_{\mathrm{rms}} = \left(\frac{2}{3}k^D_{\mathrm{corr.}}\right)^{1/2} = \left(\frac{2}{3}k^C\right)^{1/2} + \left(\frac{2}{3}k^D\right)^{1/2} \exp\left(-\frac{C_\beta^{1/2}}{St}\right)$$

$$\text{with } St = \frac{\tau_\mathrm{p}}{T_\mathrm{E}}, \quad T_\mathrm{E} = \frac{T_\mathrm{L}}{0.356} \quad \text{and} \quad T_\mathrm{L} = 0.41\frac{k^C}{\varepsilon^C} \tag{101}$$

where T_E and T_L denote the Eulerian time scale and the Lagrangian integral time scale, respectively. By increasing the value of the Stokes number (Stokes number values considered here are between 2 and 23), this modification causes an increase in streamwise turbulence level, which agrees well with the experimental observations. The magnitude of the streamwise root-mean-square value corrected in such a way agrees much better with the experimental data for the channel flow considered.

5.2. Particle-laden flow over a backward-facing step

Figure 7 displays streamwise mean velocities of both carrier gas-phase and copper particles at several locations within the recirculation zone, reattaching (experimentally obtained reattaching length is $x_\mathrm{R}/H \approx 7.5$) and recovery region. In Figure 7(a) only the results of the unladen flow are depicted. The results of the prediction of the laden flow show no noticeable difference.

In general, the velocity profiles predicted by both methods agree rather well with the experimental results. By focussing the wall region within the separation zone and reattachment, the deviations typical for eddy viscosity model application are observed. The secondary recirculation zone in the corner immediately behind the step was not predicted numerically due to well-known weaknesses pertinent to a eddy viscosity model scheme. This is due, on the one hand, to poor prediction

DOI: 10.1002/fld

of the normal stress components that are ultimately responsible for secondary flows and, on the other hand, to the use of wall functions that do not capture proper near-wall flow behavior in the recirculation zone. It results finally in a shorter main recirculation zone. In spite of these circumstances, the velocity profiles in the recovery region ($x/H = 9$ and 12) agree surprisingly well with the experiment. Similar to the channel flow, the particle velocities (Figure 7(b)) exhibit an almost uniform behavior across the flow, with a maximum value agreeing well with experimental data. However, the profile shapes deviate substantially, indicating a nearly homogeneous particle velocity field. This departure could be caused by the manner of defining the turbulent diffusion coefficients of dispersed phase in the $k-\varepsilon$ modelling concept, featuring also the turbulence kinetic energy generation. If the value of the diffusion coefficient is too low, the turbulent character of particle diffusion cannot be preserved. If the value is too high, the particle velocity field becomes nearly homogenous. On the other hand, this outcome is closely connected to the vanishing mass load Z (denoting consequently the zero value of the volume fraction α^D), the recirculation regions are usually characterized by (see Figure 8 and corresponding discussion). Oliveira and Issa [2] addressed such a situation in their study proposing a remedy (not applied at present) based on an appropriate division of the equations governing the two-phase flow by the corresponding volume fraction. The evolution of the mass loading profiles along the channel behind the step is compared only with the Euler/Lagrange calculation (Figure 8), indicating fairly good agreement. Immediately behind the step no particles exist in the Euler/Euler predictions, agreeing well with experimental observation (not shown here), in spite of the non-zero velocity field behind the step (Figure 7(a)). The velocity field represents the solution of the transport equations (25) and not of the equations describing particle motion, as in the case of the Euler/Lagrange method, in which the velocities are only obtained if particles are present. The profiles of particle concentration further downstream indicate the spreading of the dispersed phase in the cross direction due to the particle diffusion mechanism.

The flow over a backward-facing step is affected by an adverse pressure gradient due to the sudden channel expansion. It is well known that flow deceleration imposed in such a manner promotes isotropy, thus conforming closer to the $k-\varepsilon$ modelling concept. Furthermore, the velocity gradient tensor exhibits more non-zero terms in this flow configuration (in the channel flow only

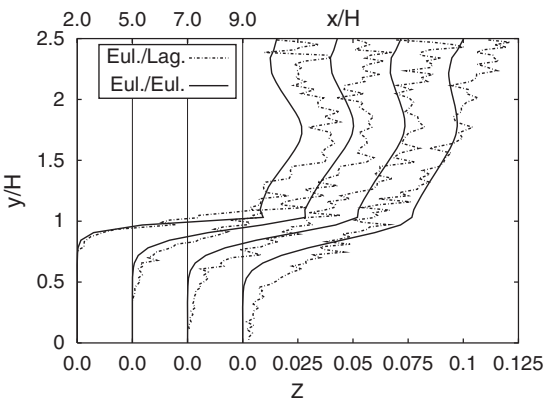

Figure 8. Profiles of mass loading at selected downstream locations in the particle-laden, backward-facing step flow.

DOI: 10.1002/fld

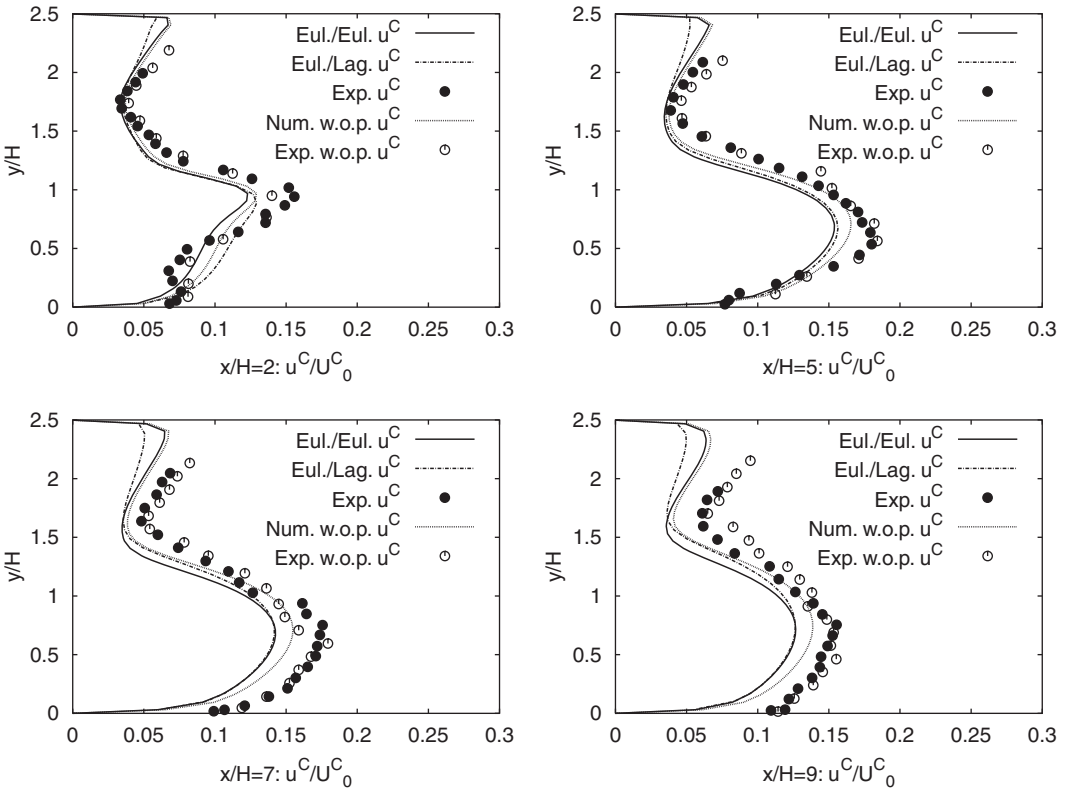

Figure 9. Streamwise turbulence intensity of the continuous phase at selected downstream locations in the particle-laden, backward-facing step flow.

mean shear exists). These circumstances contributed strongly to a generally acceptable agreement of the streamwise turbulence intensities of the gaseous phase (Figure 10). Contrary to the channel flow, no attenuation of the turbulence intensity of the gas phase was observed along the entire domain behind the step. The streamwise turbulence intensities of the dispersed phase (Figure 9) were again much lower then the measured ones. The agreement was significantly improved after their correction by the ansatz introduced in Equation (101).

The following concluding remarks can be drawn with respect to the potential of the present four equation, eddy-viscosity-based Euler/Euler model in computing the two particle-laden channel flow configurations without and with sudden expansion. The modification of the mean gas-flow field due to particle motion was very low in both flow configurations; the fact being very well reproduced by the model adopted. The magnitude of the particle velocity in the core region of the flows is predicted reasonably well, but not the low value observed experimentally in the region towards solid walls. The isotropic assumption of the turbulence model cannot cope with turbulence anisotropy. The introduction of the correction method of the streamwise particle velocity deviation improves this behavior significantly in the zones of high shear. The experimentally observed attenuation of the turbulence intensity of the gaseous phase in the fully developed channel flow was not correctly predicted. This requires further analysis.

DOI: 10.1002/fld

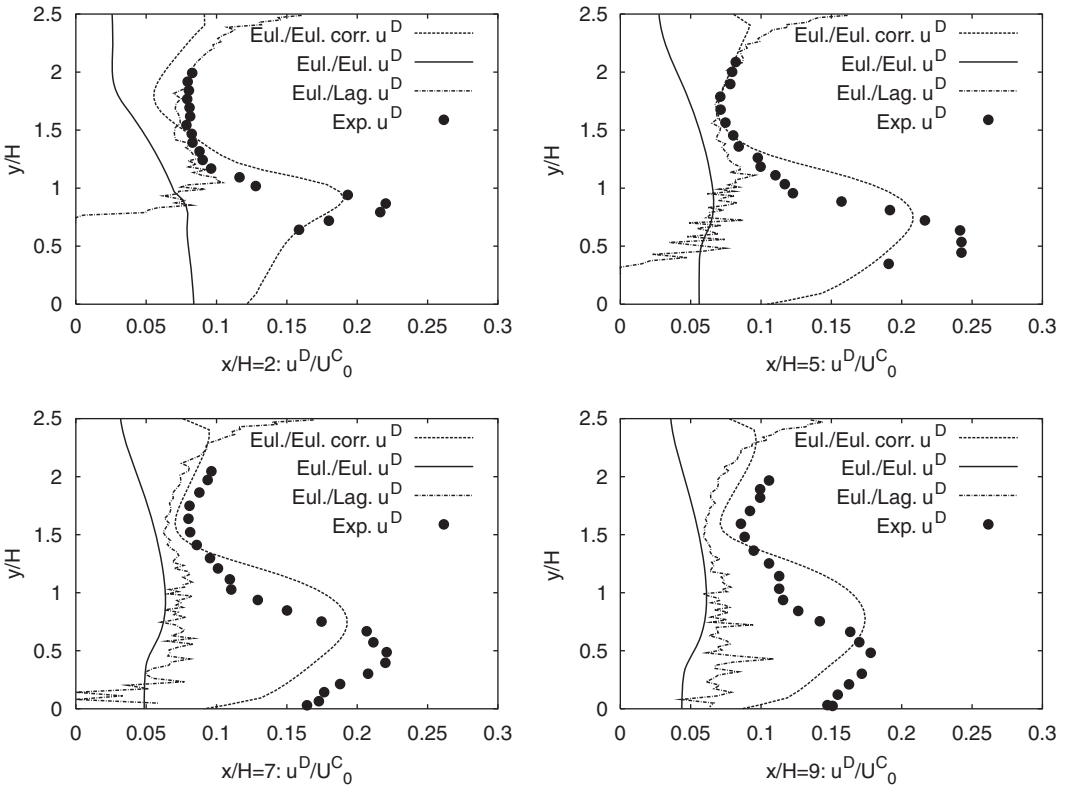

Figure 10. Streamwise turbulence intensity of the disperse phase at selected downstream locations in the particle-laden, backward-facing step flow.

6. EVAPORATION IN A TURBULENT GAS–LIQUID CHANNEL FLOW: COMPUTATIONAL RESULTS AND DISCUSSION

The flow configuration simulated, a turbulent, gas/liquid channel flow, is displayed in Figure 3 (only upper half of the duct, being discretized by ca. 66 000 grid cells, is considered). Similar to the particle-laden cases, a three-dimensional solution domain was adopted. The results obtained by the Euler/Euler computational model presented in Sections 2 and 3 were compared with the results obtained by an Euler/Lagrange method solving the transport equations of the carrier phase (Euler framework) and individual tracking of the droplet parcels (14 800 trajectories were introduced into the flow field displayed in Figure 11) (Figures 11–15). The Euler/Lagrange simulations were performed by using the commercial CFD software package AVL SWIFT (AVL List GmbH, Graz). The code employs the finite volume discretization method, which rests on the integral form of the general conservation law applied to the polyhedral control volumes. All dependent variables are stored at the geometric center of the control volume. The appropriate data structure (cell-face-based connectivity) and interpolation practices for gradients and cell-face values are introduced to accommodate an arbitrary number of cell faces. The convection can be approximated by a variety of differencing schemes. The diffusion is approximated using central differencing. The overall

DOI: 10.1002/fld

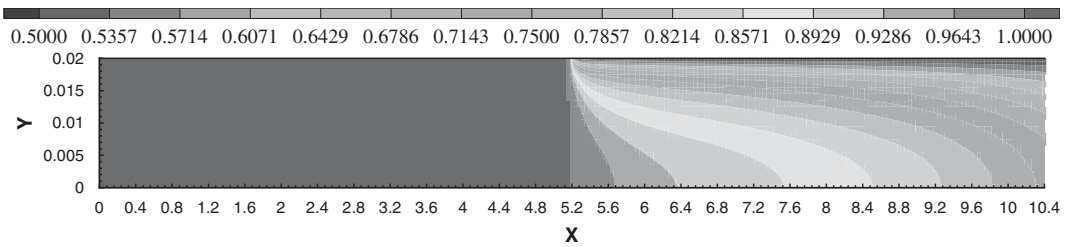

Figure 11. Isosurfaces of the relative humidity obtained by the present Euler/Euler scheme.

solution procedure is iterative and is based on the SIMPLE-like segregated algorithm, which ensures coupling between the velocity and pressure fields. The Euler/Lagrange method used here involves several submodels accounting for turbulence dispersion (influence of the gas-phase turbulence on the particulate phase by introducing the eddy life time), droplet coalescence/collision, secondary break-up, wall interaction and finally evaporation. The flow field is modelled by the RANS method coupled with the eddy viscosity model equations. The wall closest numerical nodes were situated at $y^+ \geqslant 28$.

The boundary conditions of the flow configurations considered (channel dimensions, bulk Reynolds number, turbulence intensities, etc.) correspond to the geometry used for the experimental investigation of the particle-laden flow by Kulick *et al.* [29]. Instead of solid particles, the flow was laden with droplets characterized by their uniform distribution along the entire inlet cross-section. This flow configuration (no experimental data for the evaporation process exist) with the mass loading of the liquid phase being set to $Z = 1\%$ is simulated, corresponding to a dilute liquid/gas two-phase flow. As already noted, the present evaporation model was assessed by contrasting the Euler/Euler results to the results of the Euler/Lagrange method exclusively. Admittedly, the comparison with an appropriate experimental database would be more appropriate. However, the experimental investigations of droplet evaporation are very rare. The most widely used experimental study for the model validation is the one by Qiu and Sommerfeld (we discussed this experiment and the complementary Euler/Lagrange computations in the introductory section, [23]). Unfortunately, this experimental study does not provide details about the temperature and relative humidity fields, Nusselt number distribution, evaporation time scale, etc. that one should have to thoroughly validate the present model. Furthermore, this experiment was designed following closely the Euler/Lagrange approach especially with respect to the disperse phase inflow data and droplet parcels tracking procedure. To avoid any ambiguity in regard to the definition of the inlet data for the Euler/Euler method (traditionally, the so-called settling length occurs, along which the model equations adjust to the prescribed experimentally inlet results) we preferred the numerically determined, fully developed inflow conditions generated by using the same Euler/Euler method being applied for the evaporation computations. Accordingly, we accomplished the results validation by comparing them with the results obtained by employing the same Euler/Lagrange method as it was used in the study of Sommerfeld *et al.* [23]. Keeping in mind the well-known performance of the aforementioned Euler/Lagrange scheme, we believe that the predictive capabilities of the present evaporation model can also be plausibly assessed in the framework of a pure computational analysis.

Figures 11–15 show some selected results obtained by both approaches. In order to provide the fully developed flow and turbulence conditions, a completely saturated gas phase (relative

DOI: 10.1002/fld

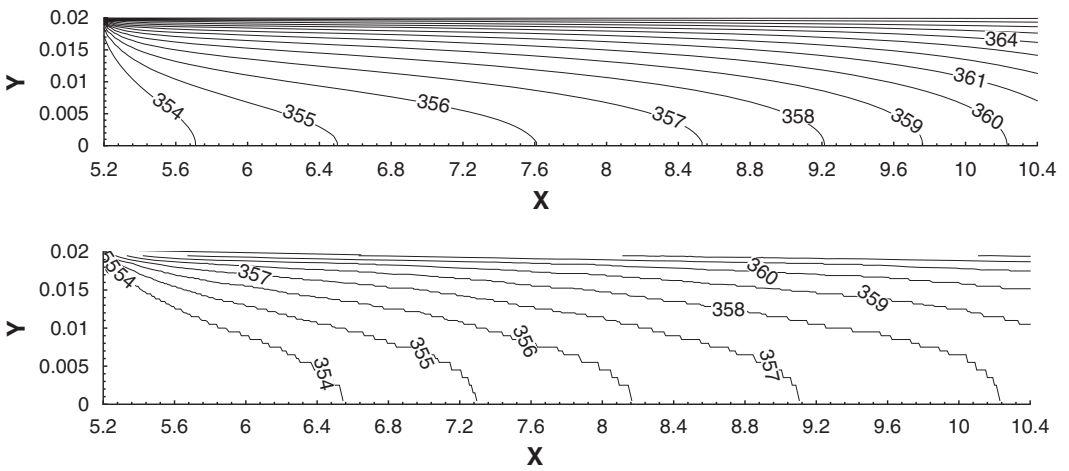

Figure 12. Comparison of the gas temperature fields obtained by the present Euler/Euler scheme (upper) and the Euler/Lagrange method (lower).

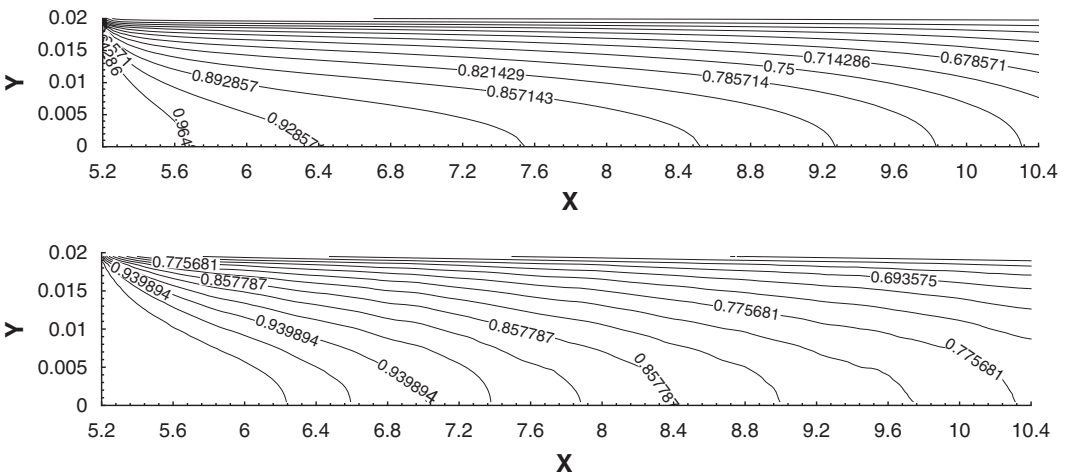

Figure 13. Comparison of the relative humidities obtained by the present Euler/Euler scheme (upper) and the Euler/Lagrange method (lower).

humidity was taken to be 100%, large dark area in Figure 11) was computed over the duct length of $260h = 5.2\,\mathrm{m}$ (h-channel half-width), prior to the onset of the evaporation process. The liquid phase evaporation was introduced by heating the duct walls (in such a manner the temperature derivative[§] corresponding to the difference between 353 K prescribed at the inlet cross-section—$x = 0$—and the constant wall temperature of 368 K was imposed, Figure 12) causing a decrease in

[§]The temperature range ($T < 100°\mathrm{C}$) was chosen to prevent complete evaporation. The study focussed primarily on the evaporation process due to concentration gradient. The temperature range prescribed corresponds to the high saturation pressure derivative $\mathrm{d}p_{\mathrm{sat}}/\mathrm{d}T$ (i.e. $\mathrm{d}Y_{\mathrm{sat}}/\mathrm{d}T$).

DOI: 10.1002/fld

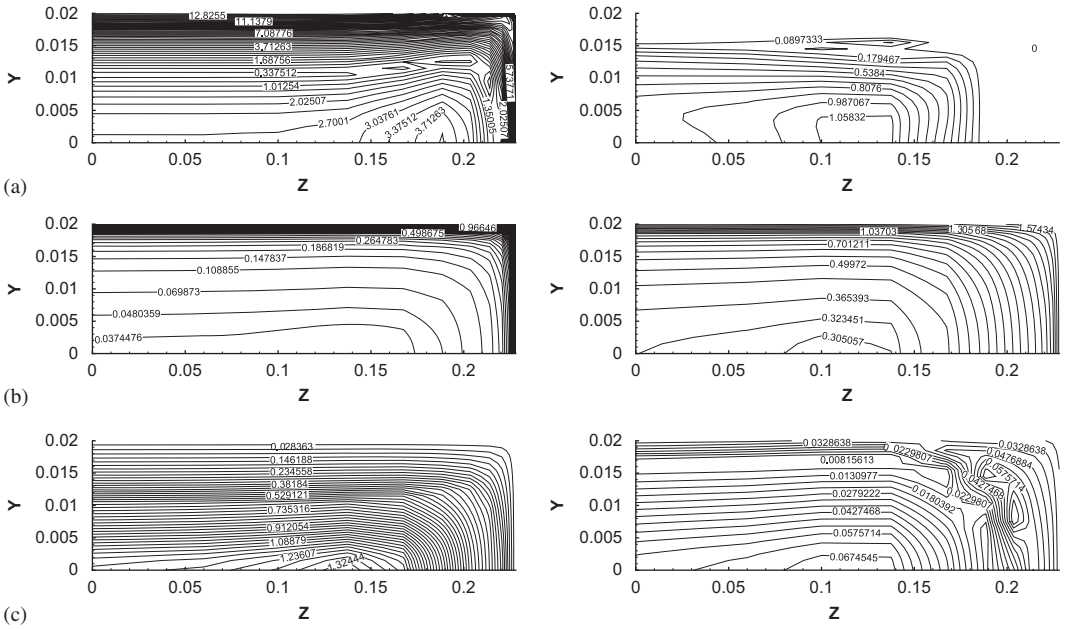

Figure 14. Isolines of (a) Reynolds number Re_{rel}, (b) mass transfer coefficients B_{M} and (c) time scale of evaporation τ_{Γ} across the duct at two selected longitudinal locations $x/h=20$ (left) and 140 (right) obtained by the present Euler/Euler scheme.

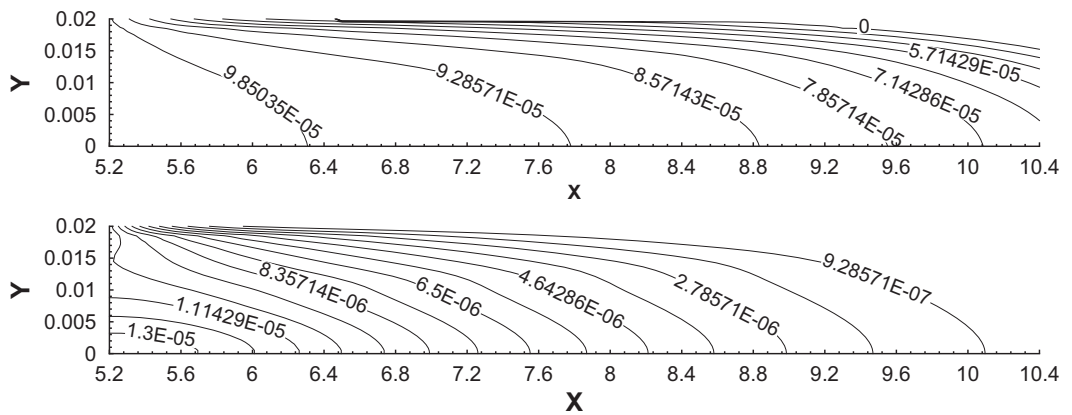

Figure 15. Droplet diameter (upper) and volume fraction α^{D} (lower) isolines obtained by the present Euler/Euler scheme.

the relative humidity (Figure 13). A somewhat slower penetration of the heat flux into the flow core (Figure 12, lower), obtained by the Euler/Lagrange method in conjunction with original evaporation model of Abramzon and Sirignano [22] implemented in the AVL SWIFT commercial flow solver, causes weaker temperature gradients in this region, leading to a less intensive evaporation process,

DOI: 10.1002/fld

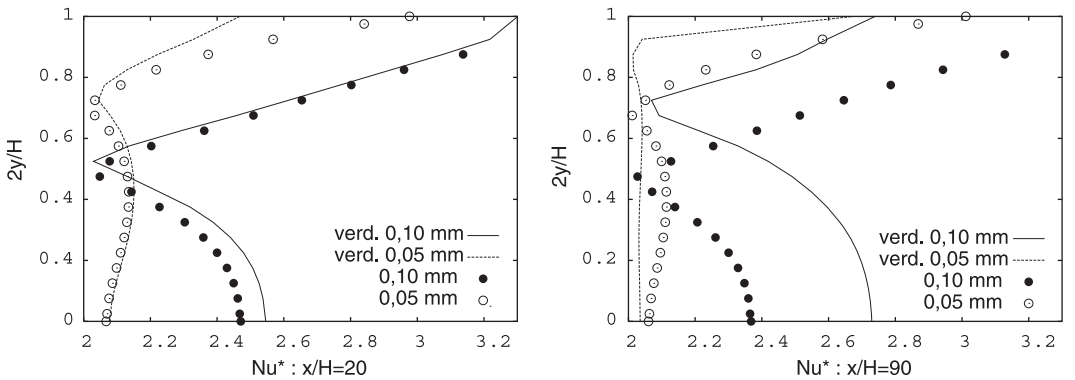

Figure 16. Modified Nusselt number at two selected locations: $x/h = 20$ and 90.

a fact represented by a slightly higher vapor concentration (weaker decrease from the initial 100%, Figure 13 lower). Figure 14(a) shows the isolines of the relative Reynolds number (important for the determination of the drag force relaxation time scale τ_p in the volume fraction weighted momentum equation for the continuous phase) based on the velocity difference $|\mathbf{u}^C - \mathbf{u}^D|$ and droplet diameter D_p in the right top quarter of the duct cross-section at two selected longitudinal locations. The results confirm the general reduction of the Reynolds number due to the droplet evaporation (diameter reduction and consequently the volume fraction α^D reduction, Figure 15). This tendency is particularly pronounced in the near-wall flow regions. Figure 14(b) displays the evolution of the mass transfer coefficients B_M in the Abramzon and Sirignano evaporation model. This coefficient, representing indeed a measure of the vapor fraction being absorbed by the surrounding gas phase, increases due to warm up of the gas phase. The ratio of the droplet surface to the droplet volume increases by the droplet diameter reduction. Owing to the temperature raise, resulting in the intensification of the evaporating process, the time scale of the evaporation decreases (Figure 14(c)). Figure 16 illustrates the influence of the evaporation (non-evaporating liquid phase was also computationally simulated) and droplet diameter (two different D_p-values were analyzed: 50 and 100 μm) on the Nusselt number redistribution across the channel. Although no significant changes in the Nusselt number behavior in the case without evaporation (symbols) are noticed, the modified Nusselt number exhibits a decrease in the region with the dominating influence of the small droplets (near wall) if the evaporation is accounted for (lines). In contrast, the increasing effect of the modification (in terms of the Reynolds number, Figure 11(a)) is pronounced in the flow core.

7. CONCLUSIONS

The potential of a four-equation model of turbulence, based on the eddy viscosity concept for the two-phase flow simulation in the framework of the Euler/Euler approach, is investigated by computing particle-laden flow in a plane and suddenly expanded channel configurations and evaporation in a turbulent gas–liquid flow in a three-dimensional duct. The overall agreement between results of the present Euler/Euler method with available experimental data and the Euler/Lagrange simulations performed in parallel is satisfactory.

DOI: 10.1002/fld

The distribution of the volumetric fraction of the dispersed phase obtained by solving an appropriate model equation indicated a local decrease within the separation bubble in the particle-laden, backward-facing step flow, agreeing well with the Euler/Lagrange simulation results. The particle velocity variance, modelled in line with the turbulence structure of a single-phase flow, features the coefficient of the particle diffusion model. The results concerning the mass loading of the dispersed phase obtained in the regions with strain rates of increased complexity, as e.g. in recirculating regions and separated shear layers, compare well with the outcome of the Euler/Lagrange scheme.

The simulation of the liquid mass decrease in an evaporating gas/liquid flow is based on a vaporization-rate-dependent behavior of the droplet size distribution function. A transport equation for a newly defined variable, called phase-interface surface fraction, quantifying the droplet surface size change was introduced and tested in conjunction with Abramzon and Sirignano's evaporation model. The decreasing rate of liquid mass and drop cloud surface is modelled based on the d^2-law. The prediction of wall-temperature-dependent decrease in relative humidity near the wall and the induced vaporization rate give results similar to those obtained in the Euler/Lagrangian simulation of the vaporization process.

ACKNOWLEDGEMENTS

The cooperation with AVL List GmbH, Graz, Austria, is gratefully acknowledged. The Euler/Lagrange results of the evaporating particle-laden channel flow are taken from simulations of Kristijan Horvat. We also thank Dr Gangolf Kohnen for making his Euler/Lagrange results of the particle-laden flows available.

REFERENCES

1. Politis S. Prediction of two-phase solid–liquid turbulent flow in stirred vessels. *Ph.D. Thesis*, Imperial College, London, 1989.
2. Oliveira PJ, Issa RI. Numerical aspects of an algorithm for the Eulerian simulation of two-phase flow. *International Journal for Numerical Methods in Fluids* 2003; **43**:1177–1198.
3. Lopez de Bertodano M, Lee SJ, Lahey RT, Drew DA. The prediction of two-phase turbulence and phase distribution phenomena using a Reynolds stress model. *Journal of Fluids Engineering* (ASME) 1990; **112**:107–113.
4. Lance M, Marie JL, Bataille J. Homogeneous turbulence in bubbly flows. *Journal of Fluid Engineering* (ASME) 1991; **113**:295–300.
5. Chen X-Q, Pereira JCF. Computation of turbulent evaporating sprays with well-specified measurements: a sensitivity study on droplet properties. *International Journal of Heat and Mass Transfer* 1996; **39**(3):441–454.
6. Vit C, Flour I, Simonin O. Modelling of a confined bluff body flow laden with polydispersed solid particles. In *Two-Phase Flow*: *Modelling and Instrumentation*, Celata GP *et al.* (eds). Edizioni ETS: Pisa, 1999; 1877–1884.
7. Jones WP, Launder BE. The prediction of laminarization with a two-equation model of turbulence. *International Journal of Heat and Mass Transfer* 1972; **15**:301–314.
8. He J, Simonin O. Non-equilibrium prediction of the particle-phase stress tensor in vertical pneumatic conveying. *ASME FED*, *Gas–Solid Flows* 1993; **166**:253–263.
9. Clift R, Grace JR, Weber ME. *Bubbles*, *Drops and Particles*. Academic Press: New York, 1978.
10. Crowe CT, Sommerfeld M, Tsuji Y. *Multiphase Flows with Droplets and Particles*. CRC Press LLC: Boca Raton, London, 1998; 471. ISBN 0849394694.
11. Crowe CT, Chung JN, Trout TR. Particle mixing in free shear flows. *Progress in Energy and Combustion Science* 1988; **14**(3):171–194.
12. Schiller L, Naumann A. Über die grundlegenden Berechnungen bei der Schwerkraftaufbereitung. *VDI-Zeitschrift* 1933; **77**:318.
13. Yuen MC, Chen LW. On drag of evaporating liquid droplets. *Combustion Science and Technology* 1976; **14**: 147–154.
14. Grad H. On the kinetic theory on rarefied gases. *Communications on Pure and Applied Mathematics* 1949; **2**(4):331–407.

DOI: 10.1002/fld

15. Berlemont A, Benoist F, Gouesbet G. Influence of collisions on particle fluctuation velocities using Lagrangian approach. *Numerical Methods in Multiphase Flows* (ASME) 1994; **185**:23–28.
16. Jenkins JT, Richman MW. Grad's 13-moment-system for a dense gas of inelastic spheres. *Archive for Rational Mechanics and Analysis* 1985; **87**:355–377.
17. Csanady GT. Turbulent diffusion of heavy particles in the atmosphere. *Journal of the Atmospheric Sciences* 1963; **20**:201–208.
18. Loth E, Tryggvason G, Tsuji Y, Elgobashi SE, Crowe CT, Berlemont A, Reeks M, Simonin O, Frank Th, Onishi Y, van Wachem B. Multiphase flow modelling. In *Multiphase Flow Handbook*, Crowe CT (ed.). Taylor & Francis: London, 2005; 13.1–13.150.
19. Renksizbulut M, Yuen MC. Experimental study of droplet evaporation in a high-temperature air stream. *Journal of Heat Transfer* (ASME) 1983; **105**:384–388.
20. Park TW, Aggarwal SK, Katta VR. Gravity effects on the dynamics of evaporating droplets in a heated jet. *Journal of Propulsion and Power* 1995; **11**(3):519–528.
21. Ranz WE, Marshall WR. Evaporation from drops: parts I & II. *Chemical Engineering Progress* 1952; **48**:141–146, 173–180.
22. Abramzon B, Sirignano WA. Droplet vaporization model for spray combustion calculations. *International Journal of Heat and Mass Transfer* 1989; **32**:1605–1618.
23. Sommerfeld M, Kohnen G, Qiu HH. Spray evaporation in turbulent flow: numerical calculations and detailed experiments by phase-Doppler anemometry. *Revue de Institut Francais du Petrole* 1993; **48**(6):677–695.
24. Aggarwal SK, Park TW. Dispersion of evaporating droplets in a swirling axissymmetric jet. *AIAA Journal* 1999; **37**(12):1578–1587.
25. Klingsporn M, Renz U. Numerical modelling of diesel spray vaporization. *Twenty-seventh International Symposium on Automotive Technology and Automation*, Aachen, 1994; 815–822; 94SU037.
26. Gosman AD, Clerides D. Diesel spray modelling: a review. *Proceedings of the International Conference on Liquid Atomization and Spray Systems—ILASS Europe*, Florence, Italy, 9–11 July 1998.
27. Kolaitis DI, Founti MA. A comparative study of numerical models for Eulerian–Lagrangian simulations of turbulent evaporating sprays. *International Journal of Heat and Fluid Flow* 2006; **27**:424–435.
28. Sommerfeld M, Qiu HH. Experimental studies of spray evaporation in turbulent flow. *International Journal of Heat and Fluid Flow* 1998; **19**:10–22.
29. Kulick JD, Fessler J, Eaton JK. Particle response and turbulence modification in fully developed channel flow. *Journal of Fluid Mechanics* 1994; **277**:109–134.
30. Fessler J, Eaton JK. Turbulence modification by particles in a backward facing step flow. *Journal of Fluid Mechanics* 1999; **394**:97–117.
31. Kohnen G. Über den Einfluss der Phasenwelchselwirkungen bei turbulenten Zweiphasenstroemungen und deren numerische Erfassung in der Euler/Lagrange Betrachtungsweise. *Dissertation*, Shaker Verlag: Aachen, 1997; ISBN 3-8265-3175-2.
32. Deutsch E, Simonin O. Large-eddy simulation applied to the motion of particles in stationary homogeneous turbulence. *ASME FED* 1991; **110**:35–42.
33. Oliveira PJ. Computer modeling of multidimensional multiphase flow and application to T-junctions. *Ph.D. Thesis*, Impirial College, London, 1992.
34. Groll R, Jakirlić S, Tropea C. Two-equation diameter-PDF transport modelling of an evaporating poly-dispersed droplet-laden flow. *Proceedings of the International Conference on Liquid Atomization and Spray Systems—ILASS Europe*, Nottingham, U.K., 6–8 September 2004.
35. Kastner O. Theoretische und experimentelle Untersuchungen zum Stoffübergang von Einzeltropfen in einem akustischen Rohrlevitator. *Dissertation*, Technische Fakultät der Universität Erlangen-Nürnberg, 2001.
36. VDI-Wärmeatlas. *Berechnungsblätter für den Wärmeübergang*. VDI-Verlag GmbH: Düsseldorf, 5-te erweiterte Auflage, 1988. ISBN 3-18-400760-X.
37. Atkins PW. *Physikalische Chemie*. VHC Verlagsgesellschaft: Weinheim, 1990.
38. Hubbard GL, Denny VE, Mills SF. Droplet vaporization—effects on transient and variable properties. *International Journal of Heat and Mass Transfer* 1975; **18**:1003–1008.
39. Lucas K. *Thermodynamik*. Springer: Berlin, Heidelberg, 1995.
40. Groll R. Numerische Modellierung der Verdunstung turbulenter Zwei-Phasen-Strömungen mittels eines Euler/Euler-Verfahrens. *Dissertation*, Darmstadt University, Shaker Verlag: Aachen, 2002; ISBN 3-8322-0652-3.
41. Issa RI, Oliveira PJ. Accounting for non-equilibrium turbulent fluctuations in the Eulerian two-fluid model by means of the notion of induction period. *Proceedings of the 3rd International Conference on Multiphase Flow ICMF'98*, Lyon, 1998.

DOI: 10.1002/fld